AMT-8-C158-2015

Author response to referee's comments

Anonymous Referee #1

General comments

The presented study is highly relevant for improving the understanding of thermal properties of urban areas. It addresses one of the main challenges in observing long-wave radiation or surface temperatures of cities from different platforms: the implications of viewing geometry. An innovative approach was taken to generate a dataset from a real urban setting using a combination of creative measurements and data analysis. This unique dataset allows for critical issues such as thermal anisotropy and sensor viewing geometry to be analysed. Important conclusions are drawn that are relevant for observations of similar urban surface types. In general, the work is very well presented including well-designed figures, however, some minor aspects (especially regarding the role of material properties) should be discussed more consistently.

We appreciate the positive feedback on the approach and acknowledge this very careful review. Thank you very much. We have addressed the aspect regarding material properties in our answers to the specific comments below.

Specific comments

Although Kup is the shortwave radiation reflected at the surface, it is better not to call it 'shortwave reflectance' as this terms usually refers to the ability of the surface to reflect radiation, i.e. the ratio of Kup/Kdn.

We acknowledge that the term could be misinterpreted.

→ We have therefore changed all instances of 'shortwave reflectance' in the text to 'reflected shortwave radiation'. The same has been applied to 'longwave reflectance' that was changed to 'reflected longwave radiation' (see also second reviewer's comments).

Page 1898, line 19: Comment on the spectral discrepancy between the FLIR and the CNR1.

The Thermovision A40M has a sensitivity mostly in the 'atmospheric window' region as shown in figure R1, with > 50% from 8.1 µm to 14.6 µm, and the highest sensitivity between 9.2 µm and 11.8 µm (> 90%) (Source: Flir Systems, pers. comm., 2011). The curve in Figure R1 was used for the atmospheric correction. The CNR-1 four component radiometer hosts two CG3 pyrometers that quantify $L\downarrow$ and $L\uparrow$. The CG3 are broadband instruments in the long-wave, sensitive in the spectral range from 5 to 50 µm (Campbell Scientific, https://s.campbellsci.com/documents/ca/manuals/cnr1_man.pdf, accessed May 20, 2015).

→ We described the Thermovision A40M more precisely in the manuscript "The microbolometer is sensitive to thermal infrared radiation between 7.5 to 15 µm although highest sensitivity is concentrated between 9.2 and 11.8 µm (> 90% sensitive)."

→ We added a description of the CG3 as follows: "Shortwave irradiance ($K\downarrow$) and reflected shortwave radiation ($K\uparrow$) were measured using two CM3 pyranometers, and longwave irradiance ($L\downarrow$), and the sum of emitted and reflected longwave radiation ($L\uparrow$) were quantified using two CG3 pyrgeometers (spectral sensitivity from 5 to 50 µm), all at 5 min temporal resolution."

This difference does not affect our results, because we do not compare CNR-1 and FLIR Thermovision A40M exactly for the reason that they represent different spectral bands. When simulating a hemispherically calculated $L\uparrow$ from the data observed by the FLIR Thermovision A40M we specifically exclude the atmospheric effects and state that the calculated surface temperature is the only factor affecting emittance in the simulations. The measured $L\uparrow$ from a real pyrgeometer at different heights, of course, would additionally be impacted by the atmospheric effects between the surface and the measurement level.

→ We added the following clarification to the manuscript: "The simulated hemispherical sensor signals exclude any atmospheric effects and only consider emittance, and treat the surface as a black body. Note that measured L_h from a real broad-band pyrgeometer at different heights would additionally be impacted by atmospheric effects between the surface and the measurement level that are not considered in the current study."

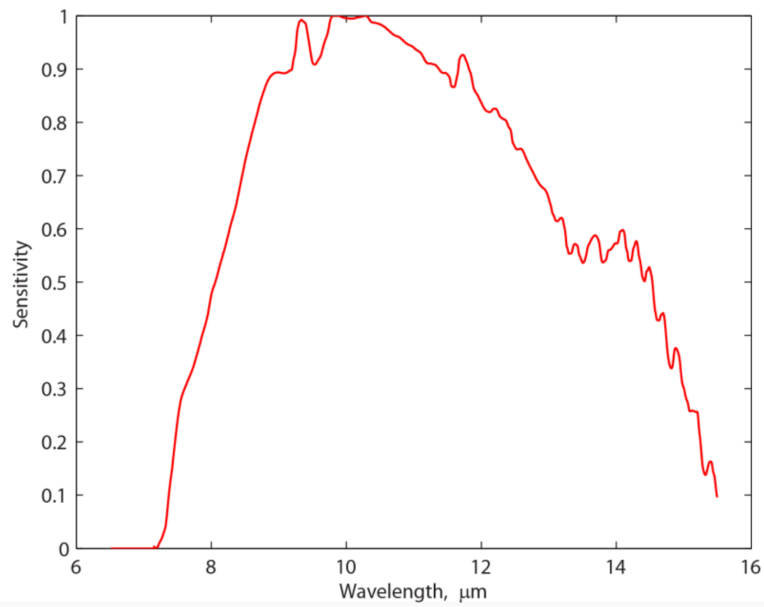

Figure R1 – Typical spectral response curve for a Thermovision A40M. Some variation between instruments is expected (Source: FLIR Systems).

Page 1900, line 6: Comment on the uncertainty from manual material identification for emissivity detection. Was there any ambiguity? Specifically comment on material class 'paint'. Given the large fraction of walls being this material class, it is quite critical to understand potential emissivity variations. How did you define the emissivity of the paint? Given emissivity of paint can vary immensely, detection 'by eye' may introduce errors. Are all walls painted with the same paint? Also, there are many types of 'rock' and stucco can have various compositions, how did you determine the emissivity value? The emissivity of aluminium can change with finishing and can also be effected by age and weathering, please comment on the state of the materials. It would be good to see a short sensitivity test on the impact of emissivity values assigned on the complete surface temperature.

We determined emissivity based on matching materials subjectively from high resolution photographs to an emissivity table. All materials were assumed to be relatively pristine.

State and weathering of materials were not evaluated. This is a potential source of error. However, also buildings are very uniform, all have all been built between 1971 and 1976 without major retrofitting (although roof work is likely). At least, the uniformity of the age of all buildings means that there is no a priori reason for a 'historical' bias due to aging and weathering that affects anisotropy at the neighborhood level (as would be the case if buildings on one side of the street were significantly older than the other side).

→ We added the following sentence to acknowledge this as a potential source of error: 'Houses in the canyon were all built between 1971 and 1976 and are of similar dimensions and materials, with a rectangular footprint oriented perpendicular to the street and low-pitched roofs with slopes from 10º to 15º' (Section 2.1.1, 'Site') and 'Also aging and weathering of surfaces was not considered in the attribution of ε to materials'. (Section 2.2.2, Facet and material information).

Page 1901, line 5: Please comment on the accuracy of matching the USM pixels and to those of the PTST. Are you assuming a perfect overlap, i.e. no errors in the USM or the spherical tilt and azimuth angles assigned to the PTST pixels?

No, we assume an imperfect alignment. Based on manual inspection of projected panoramas errors were found. Incorrectly projected areas were mostly along edges and on distant objects. Those areas were eliminated manually and placed into the gap-filling algorithm.

→ We added the following sentence to 'Manual inspection of projected panoramas revealed some areas of incorrect attribution along edges and on distant objects. Those areas were eliminated manually and filled using a gap-filling algorithm.'

Page 1901, line 16: Why is atmospheric correction highest for the road? Should it not make most impact over lawn where evaporation is higher?

For a given path length, and assuming constant relative humidity (RH) and air temperature T_a, the atmospheric correction has the highest impact for surfaces that have a brightness temperature T_B that is most different from T_a (replacement of surface emission with emission from the atmosphere along the path). Note that RH and T_a are globally set (they are measured in canyon and then applied to the entire domain and path length). Lawns are cooler by day (transpirative cooling) than roads, so the absolute difference between their lower T_B and the globally set T_a is less. Consequently, at same path length, the impact of the atmospheric correction is less over lawns.

Page 1901, line 16: Comment on uncertainly of atmospheric correction.

There are several possible uncertainties associated with the atmospheric correction:

- The error associated to air temperature (T_a) and relative humidity (RH) inputs. T_a and RH are affected by (a) instrument error and/or (b) are not constant / representative across the entire domain (as assumed). The maximum sensitivity of the atmospheric correction to an error in RH is 0.51 K for a 10% uncertainty in RH (for the longest path length of 75m, and with the highest T_B of 44 K during midday). For air temperature, the maximum error is 0.70 K for a ±5K uncertainty in T_a (again for the longest path length of 75m, and with the highest T_B). The typical instrument errors of a HMP35A are <0.2K for T_a and <±2% for measured RHs (Campbell Scientific Inc.). The instrument errors are hence not a relevant source of error, more than an order of magnitude smaller than the values estimated above. More relevant is the assumption that the signals of T_a and *RH* are not representative for the atmosphere along the entire path / domain (lapse rate etc.). Errors of ±5K and ±5% are however unlikely at this scale, in particular during day when air is well mixed by buoyancy (daytime wind at 30 m was measured 1-3 m/s, measured variability of 1-minute air temperature in canyon was <±1K during daytime).
- Secondly, the approach of using a LUT with discrete values and the lack of an interpolation (except for T_b) might be also relevant in some cases. For example distance is attributed in 10 m increments, T_a in 2 K increments and RH in increments of 5%. This adds uncertainties for pixels that lie in-between those boundaries, but the error is symmetric.
- Another error source is that actual aerosol and trace-gas concentrations along the path may be different than assumed in MODTRAN. We use the standard atmosphere in MODTRAN. Most relevant are carbon-dioxide (CO_2.) and aerosols. The average mixing ratios of CO_2 were elevated in the urban atmosphere at the time of the experiment (408 ppm measured at 30m on nearby tower "Vancouver Sunset" during study period, hourly min: 376 ppm at 18:00, max: 445 ppm at 06:00). No information is available on aerosol enrichment.
- Finally, an uncertainty is associated with the spectral response curve of the Thermovision A40M. We used the spectral response shown in figure R1 as supplied

by Flir Systems. However, variation due to changes in lens coating and detector design are possibilities.

Page 1901, line 19: reference for equation 1

This is the broad-band equation for $L_{\uparrow}$, such as found in many micrometeorological text-books. For example in T.R. Oke, 'Boundary Layer Climates' (1987), Equation 1.13 (pg. 22) shows that the broad-band longwave flux density $L_{\uparrow}$ observed a surface is the sum of emittance (first term on r.h.s) and long-wave reflected radiation (second term on r.h.s.):

$$L_{\uparrow} = \varepsilon\sigma T_0^4 + (1-\varepsilon)L_{\downarrow}$$

If we substitute $L_{\uparrow}$ as σT_B^4 and rearrange then

$$\varepsilon\sigma T_0^4 = \sigma T_B^4 - (1-\varepsilon)L_{\downarrow}$$

Solving for T_0 results in our equation 1:

$$T_0^4 = \sqrt[4]{\frac{\sigma T_B^4 - (1-\varepsilon)L_{\downarrow}}{\varepsilon\sigma}}$$

→ We expanded the text, explained the derivation of this equation (as here) and added a reference to Oke (1987).

Page 1902, line 4: Is it correct that you approximate the canyon radiance based on the complete surface temperature? Would that not over-/underestimate the radiance incoming onto a wall or ground pixel given these actually do not 'see' the roof facets? Also, if the complete surface temperature is taken as a basis for canyon radiance, this does not take into account the distance of the facets to each other. For example, the walls will have most incoming radiance from the adjacent lawn rather than the road in the middle of the canyon and probably only little radiation is emitted between east and west facing walls given the large width of the canyon. Similarly, the lawns probably do not receive any radiation from the adjacent road. Please comment on the uncertainty associated with the assumption that relative location and distance of the facets is neglected.

The reviewer is correct that a pixel-by-pixel correction would be a more accurate approach, but this would be computationally very consuming (as the correction is iteratively applied). We argue that our approximation is probably the most reasonable approach, but cannot provide an error estimate, as we do not have the code or computer resources to calculate a pixel specific calculation for the entire domain. Maybe a canyon-only temperature (vs. including roof top temperatures) might be a compromise better for wall and floor corrections.

Page 1902, line 12: Given the buildings are located in close distance to each other, how well does the PTST actually sample the south and north facing walls?

The mean E-W wall visibility is 46% based on all houses within the domain. It is low primarily because the backs of buildings are not seen. If backs of buildings are omitted, it is 71%. With regard to the south and north facing walls, the sampling is good in the 4 houses near the scanner (~90% coverage). However it is poor (<10% coverage) for the houses further away. So for S and N walls, the statistical gap filling relies substantially on the walls 4 houses near the scanner.

→ The following text has been added: "The mean visibility of roofs and ground in the entire domain are 95% and 72%, respectively. The visibility of E-W walls is only 46% (lane-facing walls of buildings cannot be seen). For N-S walls, the visibility is good in the four nearest houses (~90%), however it is very poor (<10%) for all houses further away."

Page 1902, line 24: This is to say that the difference in SVF needs to be below the threshold? Say this explicitly.

Yes.

→ Reworded to "The pixels selected to statistically fill had to experience a difference in ψ_{sky} of less than 0.03 to the target pixel"

Page 1903, line 7: What are the implications of this gap-filling procedure? Comment on the variability of surface temperature within one pixel class, i.e. at a given time how do temperatures differ between pixels with the same facet type, material type, orientation, and SVF? Probably ground pixels also require gap filling, e.g. for areas obstructed by buildings? How do you address the fact that ground surface to the east or west of a building exhibits different shading patterns during the day? Is this incorporated? How do you deal with the case if multiple replacement pixels are available but with a differing temperature? Do you use the average?

The variability of surface temperature within one pixel class for selected facets can be found in Table 3 (values in brackets are standard deviations).

We use the average of all pixels, if multiple pixels are found. Ground surface shading was not modeled and not considered, certainly this adds a layer of uncertainty and could be an area of future improvement. At the same time it would add complexity in terms of determining shadow edges and shadow history.

→ We added 'Also, the gap-filling algorithm could be improved by incorporating the effects of facet shading and shading history, which are both currently not considered as selection criteria in the search for similar cases to fill gaps'.

Page 1905, line 12: Why is the number of pixels per diameter fixed? Should this not vary with sensor height?

The number of pixels refers to the resolution of the rendered field of view (for an example see Figure 4b), not the pixel resolution at the surface. The need for a higher resolution would be given if the pixels within the diameter could not appropriately sample the surface of interest. There is no evidence that even with the highest sensors we cannot resolve the urban surface properly (see again Figure 4). We do agree that the resolution needs to be high enough to render truthfully the relevant facets of the urban surface. This is given in the current case.

→ Expanded "Each sensor's projected FOV was rendered to a single frame 256 x 256 pixel array […]. This was determined a high enough resolution to render truthfully all relevant facets of the urban surface even for sensors at the highest locations.'

Page 1906, line 16: reference other studies discussing variations in roof temperature.

- Masson *et al.* 2002 test a model vs. observations in Mexico City and Vancouver. Their Figure 6 is an ensemble plot for a roof in the light industrial area in Vancouver with a diurnal range of roof surface temperatures of 40 K (but just one roof). The Mexico City roof temperature is in their Figure 3 and has a smaller range of about 25 K.

- Chudnovsky *et al.* 2004 (Energy Build.) quantify the maximum difference in roof temperatures between day and night at 32 K. Roofs are the facets with the highest diurnal variability.
- Christen *et al.* 2011 (Theor. Appl. Clim.) quantified an ensemble of many roofs of different materials. They show that roofs have the largest diurnal amplitude of all facets. Here temperature varied up to 31 K between ~12 h noon and ~21 h (their Figure 2).
- Salmond *et al.* 2012 (J. Appl. Meteorol. Climatol.) show roof temperatures at 1430 and 2300 in Basel, Switzerland that range from 18 to 58 K, hence a range of 40K (their Figure 5).

→ Added "Roof temperatures hence show the largest diurnal amplitude of 40 K, which is in the typical range of reported values for clear-sky days in other studies (Masson *et al.*, 2002, Chudnovsky *et al.* 2004, Christen *et al.* 2011, Salmond *et al.* 2012).

Page 1907, line 12: Please comment on the differences in night-time wall temperatures: given the surface morphology of the study area, south and north facing walls have a much lower SVF than the east and west facing walls. In theory, the latter should cool easier – why could the south facing walls have the lowest temperatures? Is this due to small scale variations in wall structure, i.e. porches etc.? Or the vegetated ground surface in the vicinity? Could the small deviation be explained by sampling bias?

This is an interesting comment. As mentioned in the text, notably, south facing walls achieve warmer 24 h temperatures of 298.5 K (±4.0 K) than others due to their sun-facing aspect, however they are coldest at night. Table 3 lists the results, whereas on average North facing walls experience 283.6 (±1.7) K minimum temperature, and South facing walls experience 282.5 (±2.0) K. The difference between North and South facing walls is within the standard deviation given. However, it is also notable that East (284.6 ±2.3 K) and West (284.3 ±1.7 K) are higher, which is at first counter-intuitive.

There are two possible explanations for the fact that S-facing and N-facing walls are colder than W and E facing walls. N/S walls lack the substantial roof overhangs and balconies, that reduce the local sky view faction in both storeys (see Figure 2 and web supplement), which imposes retarded loss at night. Secondly the difference might be affected by the fact that E/W walls have more windows that N/S walls.

After reviewing this comment, we argue it is more relevant to point out the differences between N/S and W/S:

→ Changed the text as follows: 'At night, north and south facing walls are slightly colder than west and east facing walls (Tab. 3). This can be explained by the substantial roof overhangs and balconies, that reduce the local sky view faction over the west and east facing walls and possibly the fact that east and west facing walls have more windows'

Page 1908, line 7-8: reword 'at this point a sensor with a narrow IFOV in the nadir sees mostly horizontal surfaces' – this is always the case. I think you rather want to point out that at this point, horizontal facets tend to be warmer than vertical ones, the latter being hardly sampled by the nadir sensor?

→ Corrected. We reworded line 7 "; at this time horizontal surfaces, especially those with large ψ_{sky} are warm relative to vertical surfaces and dominate the radiance received by a narrow FOV sensor.'

Page 1908, line 13: How do you explain the relative behaviour shown in Figure 5 and Figure 7? In Figure 5, the facet temperatures seem all very similar at about 9 am, one could assume that viewing geometry is least relevant at this time of day. However, best agreement between complete surface temperature and nadir view is found at 10.30 am instead as seen in Figure 7. True, at this point in time average wall temperature is close to the complete surface temperature (Figure 5) but this is the case for a much longer morning period.

This is not a contradiction because there is no direct relation between the similarity of the three facet temperatures (wall, roof, ground, i.e. how close they are in Figure 5) and the agreement between complete surface temperature $T_{0,C}$ and the directional temperature in nadir view $T_{0,d}$ as in Figure 7. Those are different considerations. The nadir view $T_{0,d}$ can be roughly approximated by $T_{0,roof}\,Fraction_{roof} + T_{0,ground}\,Fraction_{ground}$ (neglecting any non-linear effects). Hence, if the average wall temperature is roughly equal to $T_{0,C}$ as in in Figure 7, the fractionally weighted average facet temperature of $T_{0,roof}$ and $T_{0,ground}$ matches best $T_{0,C}$ when they are counteracting each other (as at 10:30 when $T_{0,roof}$ (weighted by its area) are roughly the same amount warmer as $T_{0,ground}$ (weighted by its area) is colder than $T_{0,C}$). We therefore do not see need to discuss this discrepancy between 9:30 (Figure 5) and 10:30 (Figure 7) in the manuscript.

Page 1909, line 4-5: check: 'overestimates' and 'underestimates' are misplaced

Thank you. Yes the adjectives were reversed (incorrect).

→ Corrected. We reworded line 7 "Here in half of the hemisphere, $T_{0,d}$ underestimates $T_{0,C}$ (opposed to solar position) and in the other half $T_{0,d}$ overestimates $T_{0,C}$ (same side as solar position ….'

Page 1911, line 1: Radiation observed over west lawns higher when walls are within FOV, but are the west lawns themselves also warmer? Could the higher long-wave radiation also partly be explained by warmer grass temperatures as west lawns receive more incoming shortwave radiation because they are a) not shaded and b) also receive radiation reflected by the east-facing walls?

Yes. The west lawns are warmer, on average by 2.5 K at noon (up to 5K at 9:50). By inspection of the PTST images, the lack of shadows and hence a longer period of direct irradiance in the morning are both very reasonable explanations.

→ We changed the text as follows 'the positions over the western lawn experience higher L_h due to the warmer nearby house east-facing walls and also the warmer grass temperatures on the west lawns at noon (2.5 K warmer than lawns on east side). West lawns and the east-facing walls receive more incoming shortwave radiation during the morning when they are not shaded.'

Page 1911, line 8: Point out where the 'lane' is. Not clear. According to Table 1, ground surfaces are either composed of concrete or grass, now higher radiation from roads is explained by areas being composed of asphalt – inconsistent.

→ We have added labels 'lane' and 'road' to Figure 3.

Laneways were a mix of concrete and asphalt and bare soil. We duplicated the road surface to simulate the laneway (also treating it as concrete), so the simulated material to thermal pixel mapping should be correct regardless of the original material.

→ Material attribution of lane has been added to text.

Page 1911, line 19: True, Figure 5 shows roof facets to be warmer than the ground, however, Figure 10 now reveals that this is mainly attributed to the high surface fraction of grass. Only two roof positions show higher outgoing long-wave radiation compared to the road and lane surfaces observed with the hemispherical sensor just above the surface. While Lh just above road and lane ranges between 515-530 W m-2, only the west roof at y=0 and the east roof at y=30 show similar or higher values. The remaining four curves start at/below 515 W m^{-2}. This raises the question on how much of the temperature differences is caused by geometry and shading and how much is related to material properties and other processes such as evaporative cooling. Discuss this also with respect to the applicability of your findings to other urban surface types, i.e. do you expect the same relation between roof and ground temperatures (Figure 5) in dense urban settings where less vegetation is present? Or is this behaviour representative for suburban land use only? (You mention this in the discussion on radiometer placement in Section 3.4, page 1904 – but would be good to make this more explicit during the analysis at this point already.)

Differences in temperature of the various lawns along the canyon are expected because most lawns are irrigated, and the frequency and quantity of irrigation depends on the home occupant practices. This would be a specific suburban feature of thermal variability.

Also, roof albedo is very variable along the canyon. This is discussed in detail in the response below.

→ We added a sentence on "differences in T_0 between lawns along the canyon are expected because most lawns are irrigated, and the frequency and quantity of irrigation depends on the home occupant practices."

Page 1911, line 22: Comment on the impact of roof orientation. Given the roofs are not flat and according to Figure 3 orientations vary between buildings, one could expect the buildings at x=30, y=-15 and x=30, y=15 to show higher temperatures at their east- facing roof parts in the morning?

All roofs except for the 2nd and 4th house from south (front right of Figure 3) are aligned with the gable in a W-E orientation, so they have a south facing gently sloped roof part and a north facing gently sloped roof part (Figure 3). At the time of day shown in the figure the variation of roof temperature by azimuth is likely fairly small (given the relatively low slopes of the roofs). The roof at x = 30, y = 30 appears warmer because of a larger area (there is a roof over the balcony at the back). This roof is also notably warmer at night, so that doesn't seem to suggest a larger roof area explains everything, so it could be related to either roof albedo (high), or, if the roof over the balcony is not well insulated it may be warmer than other roofs and is obstructing a view of where cold dry grass is located in other properties.

Page 1911, line 22: How do you explain the rather high peak of west lawn, y=30 temperature at about 1.5 zb? Here, the lawn temperature exceeds the roof temperature west roof, y=30. If the contribution of road surface to the lawn positions is similar across the y-locations, how can this particular lawn position show such high radiation? Also, the radiation measurement over east lawn at y=30 does not seem to respond too the adjacent warm roof (east roof at y=30). Instead, the curve is very similar to the east lawn at y=-30 where the radiation from the roof is lower by about 20 W m-2.

The west roof at y=30 is a high albedo metal roof (see Figures R3 and R4). This means this roof is likely warming less by day than other roofs. Also as mentioned above, the various lawns along the canyon are quite possibly different because lawns are irrigated, and the frequency and quantity of irrigation depends on the home occupant practices. Average brightness temperatures of sunlit lawns (only the grassed area) range from 26 – 34°C with some areas (narrow boulevard strips bordering the road) as warm as 37°C.

Page 1911, line 24: Again, please re-visit your argument on the impact of material properties on the results presented. In Section 2.4 (page 1903) it is stated that the analysis of L derived from corrected surface temperatures is not affected by emissivity or atmospheric effects, i.e. allowing isolated analysis of viewing geometry implications. Now variations in Lh are explained by differences in material composition and related emissivity (e.g. aluminium vs. asphalt for roof surfaces).

Although we performed an emissivity correction and an atmospheric correction when projecting the thermal camera data on the surface, both effects are not considered when simulating sensors. In other words, emissivity effects are removed in this work. So it is a valid point to critique this argumentation. In fact lowering the emissivity of a surface should increase the true surface temperature in daytime because the surface would less easily emit longwave radiation, so in that sense it is opposite to the explanation given. This means, to explain this behavior, the metal roof true temperature must be less for some other reason, most likely albedo. Figure R2 shows differences between metal roofs and asphalt roofs on the west side of the canyon.

Figure R2 – Photo of houses on the western side with metal roof in centre (house number 6181 at y ~ 15 m, see also Figure R4), low albedo asphalt roof to the left (6195 at *y*=0 m) and another metal roof to the right (6159 at y=30 m). Note the visual differences in brightness that likely translate to albedo differences.

→ Changed to: "This variability is driven by differences in roof materials from house to house, with asphalt roofs giving consistently higher L_h temperatures than metal roofs, likely due to differences in albedo." Note that "Material composition" is retained, but we removed the emissivity explanation.

Page 1912, line 5: The across canyon variations are much more pronounced than the east-west comparison. Can you explain the differences of lawn observations at different *y*-locations? They do not necessarily seem to be related to variations in roof temperature which are similar at y=-30 and y=0 but vary clearly at y=30 between east and west roof, whereas radiation observed above east and west lawn is most similar at y=30. Can this be explained by variations in wall temperature?

We expect both, wall temperatures and lawn temperatures to be different at different *y* locations. The presence and location of various overhangs and microfeatures along the walls is different; lawns may be irrigated or not, depending on property, and in addition there are a few houses where tall vegetation that was manually removed and gap-filled.

Page 1912, line 11: What do you mean by 'horizontal slices'? There is definitely varying behaviour across *y*-locations, e.g. radiation observed at 0.5 z_b over the east lawn at y = - 30 appears significantly lower that that observed over east lawn at $y = 0$.

Canyon slices are defined on line 22 p. 1910 "The pattern of variability between sensor positions across the canyon cross section is repeated for all three canyon slices ($y = −30$, 0, 30 m)."

→ We argue the definition on line 22, p. 1910 (previous version) along with Figure 3 is clear and does not need further explanation here, but we added a reference to Figure 3 to the statement.

As mentioned above in the response to comment on Page 1911, line 19, differences in temperature of the various lawns along the canyon are quite possible because lawns are irrigated, and the frequency and quantity of irrigation depends on the home occupant practices.

Also note that the *x*-axis in panel (b) of Figure 10 is double the resolution of panel (a) which may be magnifying smaller differences that we are not considering significant.

→ We added a note to the caption of Figure 10, saying "Note the different scales of the x-axis in panels (a) and (b)."

Page 1912, line 12: How do you explain the increase of radiation observed over roads up to 1zb? According to Figure 5 and Figure 10, road surfaces are the warmest during night-time. Increased measurement height presumably increases the fraction of grass and walls contributing to the measurement of long-wave radiation. If these are relatively cooler than the road and lane surface, should L not decrease throughout the whole profile?

Even the lowest simulated radiometer position has significant view of lawns, and lawns are dominant in the canyon (in fact slightly asymmetric, west lawns are on average 1 m wider). So the change with height must be explained by the relative weighting of walls (relatively warm) vs. average canyon surface (relatively cold because of large lawn areas).

Page 1912, line 17: How do you explain the behaviour of the profiles over roof locations during the day relative to the night-time profiles? Judging from the analysis of Figure 10a, the west roof at y=0 is made of asphalt and the west roof at y=-30 is made of metal, the one at y=30 is somewhere in the middle. Whereas during night time, roof west at y=-30 and y=0 show very similar behaviour while the west roof at y=30 emits about 25 W m^{-2} more radiation. Can this be explained by material properties?

The west roof at $y = 0$ exhibits a large change from day to night. It is correct that the house at y=0 is an asphalt roof with a low albedo (see Figure R3 and R2, most leftmost house that is fully visible). This generates high daytime temperatures. The west roof at $y = -30$ is a dark painted metal roof, with a low thermal admittance (see Figure R3). The west roof at $y = 30$ is also metal roof, but a bright one, with likely the highest albedo (Figure R3 and Figure R2, rightmost, partially visible).

Figure R3 - Aerial photo of the study domain from 2008, highlighting the difference in albedo of roof materials (Air Photo from City of Vancouver). House number 6219 is at y=-30, house number 6195 is at y=0 and house number 6159 is at y=30.

→ We expanded the discussion as follows: "Roofs have been shown to be warmer throughout the experiment in the daytime (see Figure 5), and also exhibit a range of different albedo and thermal admittance values that explain differences along the canyon and between the east and west rows." And "Above-roofs, L_h shows substantial variation depending on position along the canyon due to different daytime heating (albedo) and thermal admittance (roof insulation)".

Page 1912, line 20: How do you define the convergence of the profiles? For the daytime case, you state convergence is reached at about 5zb and at about 6zb for the night-time. Judging from Figure 10a, the spread of profiles is about 10 W m-2 at 5zb a threshold which would be reached probably below 5zb in Figure 10b. A lower nighttime value for convergence would also be more consistent with the discussion in Section 3.4.

This is indeed inconsistent. We actually used different definitions of convergence in section 3.3 and 3.4. In 3.3, convergence was defined as the height where the average of all flux densities falls within 1 W m^{-2} of the flux density at $z/z_b = 9$ (top of figure). However, in section 3.4 we used the root mean square error (RMSE) between all different profile locations as a criteria to define the convergence. We chose the height where all horizontal simulated locations fall below a RMSE of 1 W m^{-2} was the convergence height.

→ We added a consistent definition of convergence: "The 18 profiles converge near 500 W m^{-2} at $z/z_b = 7.5$ to a RMSE between all profile locations at the same height of less than 1 W m$^{-2.}$

Of course our threshold of RMSE < 1 W m^{-2} is arbitrary, but if applied to all time steps allows a relative and quantitative estimation. A more detailed discussion follows in section 3.4.

→ We have also expanded the caption to Figure 10 'Note the different scales for panels (a) and (b).'

Page 1914, line 14: How could this be explained? Could it be that the extra conversions performed for the hemispherical sensor introduce further uncertainty? i.e. L is calculated per pixel, then corrected for cosine response and averaged to one integrated value which is then converted back to a hemispherical temperature, while T0,d is averaged only?

→ There is no difference between the procedure to calculate $T_{0,d}$ and $T_{0,h}$. In both cases the radiance in the FOV of the sensor is rendered (including cosine responses) and then the rendered field is averaged and converted back to a temperature. So there is no additional uncertainly added for the hemispherical sensor, as the two types of sensors follow the exactly same procedure, in just different projections.

At 8zb how much do vertical facets contribute to the IFOV of the hemispherical sensor? Or, could there be a bias introduced by the choice of location for the hemispherical radiometers? Even though they show clear convergence at 8zb minor differences remain that could be linked to the RMSE difference of 0.4 K. Would the curves look slightly different, if Lh was determined at e.g. y=-15 and y=15?

$T_{0,h}$ is not calculated for a single simulated *x,y* position, but calculated from the ensemble average of all 18 simulated *x,y* positions at this height (8zb), so we assume that the average of all 18 sensor positions approaches the true spatial average and no bias is introduced.

→ No changes needed as we already say "(with $T_{0,h}$ being averaged at $z/z_b = 8$ over all 18 profiles). "

Also it may not so surprising that the nadir temperature provides a good representation of the complete surface temperature in the current study, given the T0,C appears to be an average between T0, roof and T0,ground with the wall temperatures being very similar to T0,C (Figure 5). In such a case sampling the walls does not make a big impact given they are very similar to the average between roof and ground. In such a case it may be more important to sample every pixel of ground and roof surfaces in detail as is done by the nadir sensor?

It might be interesting to examine more broadly the generality of this statement (i.e. are wall temperatures usually similar to $T_{0,C}$?) for different times/geometries/vegetation fractions/types. If true it might be useful. However, even if wall temperatures are close to $T_{0,C}$ this does not explain why $T_{0,d}$ at nadir is the better predictor for $T_{0,C}$ than $T_{0,h}$. Adding walls, if walls are similar to $T_{0,C}$ would not change the estimate.

Technical corrections

Page 1897, line 22: delete 'to a'

→ Corrected.

Page 1901, line 2: 'camera location'

→ Corrected.

Page 1904, line 4: 'correct model of the 3D model' – does this refer to the USM?

→ Done. We replaced the first instance of 'model' by 'surface facet' and the second one by '3D USM' to add clarity to the text.

Page 1907, line 7: reference to Figure 5

→ Corrected. We changed the reference from Figure 7 (incorrect) to Figure 5.

Page 1909, line 18: Should this reference rather be 'Fig. 8a'?

→ Not changed. Indeed, our supplement shows additional hours to Figure 8, so the manuscript is correct - it is referring to plots that go beyond the times shown in Figure 8.

Page 1909, line 24: Should this TBP be T0,d?

→ Corrected. Yes, this was a typo. It has been changed to $T_{0,d}$

Table 1: include reference for emissivity values in caption

→ Done. We added a reference to the source of our emissivity values "(Flir Systems, 2004)"

Referee #2

This paper is very interesting. It provides useful information about the bias of thermal infrared sensors, with either a small FOV or an hemispherical FOV, that observe an urban canopy at different altitudes, and under different view directions at different solar hours. As expected, at large altitudes, the acquisition of an hemispherical sensor is no more dependent on the sensor altitude. However, the paper provides quantitative information, which allows one to calculate the most appropriate altitude. This provision of quantitative results is undoubtedly a major point of the work. The work is impressive with interesting conclusions. All steps are well explained. Generally speaking, the paper is clear and well presented. Moreover, the abstract gives a good overview of the whole work. I give below some comments and advise minor corrections.

Page 1894, line 6: the sentence is not perfectly correct. Indeed, Stefan-Boltzman law links the brightness temperature and the emittance. In short, the sentence should be a bit more general.

→ We simplified the sentence as "Thermography infers T_0 using remotely measured long-wave radiance from the surface of interest". We also moved the statement on inverting the Stefan-Boltzmann law to the next paragraph.

Page 1894, line 6: For explaining the difference between brightness temperature T_b and thermodynamic temperature, the authors introduce the canopy thermodynamic temperature of $T_{0,C} = \frac{\sum_f s_f T_{0,f}}{\sum_f s_f}$. If we neglect, the impact of emissivity, one should consider $T_{0,C} = \sqrt[4]{\frac{\sum_f s_f T_{0f}^4}{\sum_f s_f}}$ instead of $T_{O,C}$. Actually, the authors adopt this approach when they initialize Equation 2.

This is an interesting and relevant point. There is a small difference between this averaging scheme based on area-averaged longwave emittance and a straight area-averaged surface temperature. We recalculated $T_{0,C}$ based on the proposed scheme and the daily difference between the two schemes is on average >0.1 K. Hourly values differ up to 0.25K. We agree that because of the non-linearity, this averaging is consistent to what we applied when simulating the sensor views. We therefore decided to choose the proposed (long-wave based) average in the revised manuscript.

→ We changed the way $T_{0,C}$ has been calculated in the manuscript. We changed the sentence to 'The complete surface temperature $T_{0,\mathrm{C}}$ can be approximated as the area-weighted $T_{0,\mathrm{f}}$ of all facets that compose an urban surface. More precisely we define it here as the surface temperature calculated from the area-weighted long-wave emission of all facets of the urban surface, which is in absence of emissivity effect (e = 1.0):

$$T_{0,C} = \sqrt[4]{\frac{\sum_f S_f T_{0f}^4}{\sum_f S_f}}$$

where S_f is the surface area of any particular facet *f*.

→ We changed Equation (6). We recalculated Figures 5, 6, 7, and 8, and a number of numeric values in the text that related to $T_{0,C}$. In some cases the difference is not noticeable, and in all cases it is minor, but for consistency the calculation above has been used.

Page 1895. For low altitude sensors, another factor contributes to the difference between $T_{0,d}$ and $T_{O,C}$: if the sensor is at low altitude, 2 surfaces with the same area but at different distances from the sensor will tend to be seen under different solid angles, with the closer one being seen under the larger solid angle.

We agree that this can be an effect with low altitude sensors, however as discussed in the manuscript all narrow FOV sensors were therefore rendered with very high distance (10^4 m) above a tiled (replicated) surface. The manuscript says 'In 3D Studio Max, a pinhole-type camera was placed facing downward at 10^4 m above the tiled surface'. At this height, the difference in distance between roofs and ground does not influence the perspective (solid angles) anymore.

Some atmosphere correction was applied. Which atmosphere parameters were used? Which gas model? Which aerosol model? How was atmosphere information available?

The gas and aerosol model used is MODTRAN 5.2. The variable atmospheric parameters are air temperature T_a and relative humidity (RH), both measured in the canyon (in addition to path-length and surface brightness temperature), while mixing ratios of other radiatively active gases (CO_2 etc.) and aerosols are kept constant. Details are also given in the response to Referee #1. Detailed information on the model can be found in Meier et al. 2011 (Meier F., Scherer D., Richters J., Christen A., 2011: 'Atmospheric correction of thermal-infrared imagery of the 3-D urban environment acquired in oblique viewing geometry'. *Atmos. Meas. Tech.*, 4, 909-922.

→ We have improved the description of all parameters used in the manuscript and refer (as previously) to Meier *et al.* 2011 for the gas and aerosol models and the details of the procedure.

The authors mention that the atmosphere correction reached 8.6 K. Was it for an unrealistic configuration such as tremendous atmosphere humidity and/or very large distance.

This was for large off-nadir angles with long path lengths (~75m) and for brightness temperatures significantly larger than air temperature, namely on the road surfaces. Figure R4 shows the magnitude of the correction on the ground surface. Table R1 shows the mean, minimum and maximum atmospheric correction for each time step. Note that the magnitude depends not only on T_a, T_B, RH and path length d_s, but also the on spectral range of the camera, so results are not transferable from one camera to another.

Table R1 – Maximum, minimum and mean atmospheric correction values for the entire model area (Source: Adderley, 2012).

Timestep	Mean Correction (K)	Minimum Correction (K)	Maximum Correction (K)
13:30	3.7	1.8	7.4
14:30	4.2	2.1	8.4
15:30	4.3	2.1	8.6
16:30	4.2	2.1	8.2
17:30	3.7	1.8	7.4
18:30	3.2	1.6	6.5
19 :30	2.8	1.4	5.6
20:30	2.5	1.3	5.0
21:30	2.5	1.3	5.0
22:30	2.5	1.3	5.0
23:30	2.2	1.1	4.4
00:30	2.2	1.1	4.4
01:30	2.1	1.1	4.2
02:30	2.0	1.0	4.1
03:30	1.6	0.80	3.3
04:30	1.7	0.82	3.4
05:30	1.6	0.83	3.3
06:30	1.5	0.70	3.0
07:30	1.7	0.82	3.3
08:30	1.9	1.0	3.9
09:30	2.0	1.0	3.9
10:30	2.8	1.4	5.5
11:30	3.0	1.5	6.0
12:30	3.8	1.9	7.4

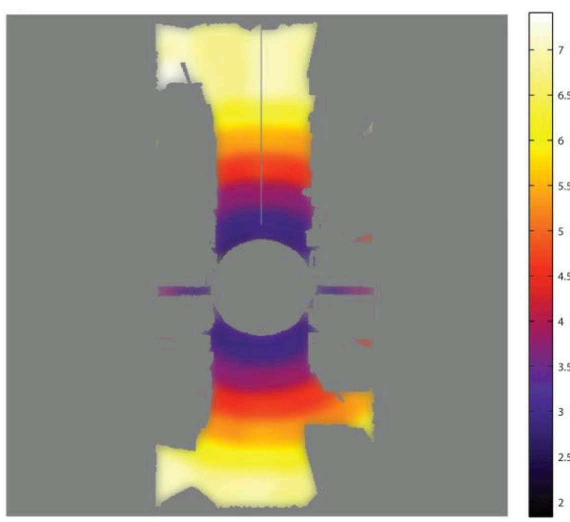

Figure R4 – Map of the effect of the atmospheric correction (in K) for the ground surface (North is up, entire domain about 100 x 100m). The concentric rings appear because of the dominant influence of the path-length d_s at this time of the day and the step-size of the distance matrix with 10 m increments (Source: Adderley, 2012).

For the atmosphere correction: - the authors pre-compute a number N of scenarios, which gives the LUT(T_B, T_a, RH). I tend to think that distance d should be also a variable parameter. Isn't it?

Yes. The distance d_s is a parameter in the correction and is part of the atmospheric correction matrix / LUT.

→ The text was enhanced by 'These corrections considered path length (d_s), local air temperature (T_a, measured in canyon), sensor measured brightness temperature T_B and relative humidity RH (measured in canyon)'. We newly also added information on resolution and range for each of the variables in the same paragraph.

If the LUT which is computed is LUT(T_B, T_a, RH, d), then it could have been more efficient to compute the 2 LUTS: $t_{atm}(T_a$, RH, $d)$ and $L_{atm}(T_a$, RH, $d)$, where t_{atm} is atmosphere transmittance and L_{atm} is the atmosphere path radiance. Indeed, one can consider that the measured radiance from a facet i is equal to:

$$L_{measure,i} = L_B(T_{B,i}).t_{atm}(T_a, \mathrm{RH}, d_i) + \mathrm{L}_{\mathrm{atm}}(T_a, \mathrm{RH}, d_i)$$

We agree with the reviewer's comment that this approach could have been more elegant, and certainly should be considered in future work. However, as the full matrix LUT (T_B, T_a, RH, d_s) has been already calculated we see no need to redo the calculation. Numerically, the result is the same.

→ No changes made to the manuscript.

In Equation 2, the authors assume that atmosphere radiance is isotropic, which is not exact. This simplifying hypothesis should be mentioned.

→ Done. We added a sentence "The approximation in Eq. 2 assumes that atmospheric irradiance is isotropic, and that the surrounding urban facets all have a uniform surface temperature equal to $T_{0,C}$."

In the work, surface emissivity is assumed to be isotropic. I did not notice that this simplifying hypothesis is mentioned in the text. If should be mentioned, if it is not.

→ Done. We added a sentence at the end of section 2.2.2. "It was assumed that ε is isotropic, i.e. that surfaces show a Lambertian behavior in the long-wave band."

Page 1906, Line 17: the word "opposite" should be replaced by "least contrasted".

→ Done. We agree with this comment and removed the word 'opposite'. We state now "$T_{0,f}$ of the ground facet shows the smallest diurnal range, with lowest $T_{0,f}$ of all facet classes during the day…". We feel "least contrasted" would be less clear.

Page 1910: the authors give tentative explanations for the difference of temperature anisotropy for different configurations (Marseille versus Vancouver). Maybe sky irradiance in the short wavelengths is another contributing factor. Indeed, if the sky irradiance is small relative to total (direct sun + Earth sky), then Earth surfaces are more isotropically illuminated, which tends to lead to more homogeneous temperatures, which tends to lead to smaller anisotropy of thermal acquisitions. Maybe, the orientation of the road is another factor.

We believe that the referee has meant "if the sky [diffuse] irradiance is large relative to" in the comment.

→ We have added a partial sentence "and potentially also differences in the ratio of direct to diffuse shortwave irradiance." to the manuscript. However all datasets compared here were done under clear-sky conditions, so differences in diffuse irradiance would not be the only factor explaining the differences.

Page 1913, Line 6: according to equation 5, RMSE = $a.e^{-b}$ if $z/z_b = 1$, and not RMSE = a.

→ Corrected. We changed the wording to "*a* is a coefficient that describes the hypothetical RMSE at ground level (z/z_b=0) in W m^{-2}" because if z/z_{b} $_{=0,}$ RMSE = 1. We also changed the following sentence to say "Practically, *a* is roughly proportional to the RMSE of T_0 of the complete urban surface"

Some terms are sometimes improperly used:

- IFOV: Instantaneous field of view. It informs on how much a single detector pixel can see in terms of field of view (FOV). Basically: IFOV=FOV/number of pixels in the direction of the FOV. In case, the sensor corresponds to a single pixel, then the terms FOV and IFOV have the same meaning. Figure 1.a is an example of ambiguous use of IFOV. It displays an image that represents the spatial extent of a surface that corresponds to the IFOV of a single detector of a satellite sensor. Page 1905, Line 3 is another example.

→ Clarified. We changed all instances of 'IFOV' to 'FOV' because in all cases we speak to the maximum spatial extent (the entire 'image') of the surface that corresponds to the sensor's signal response irrespective of the number of pixels used.

- radiance L: radiant flux emitted, reflected, transmitted or received by a surface, per unit solid angle per unit projected area. In equation 1, the term L corresponds to an emittance. Thus, page 1901, line 21, the term longwave radiation L should be replaced by longwave emittance M.

There may have been a confusion because on Page 6 we defined *L* as 'radiance' in the previous version, but mostly through the manuscript we were using *L* and the various subscripts (total longwave irradiance $L\downarrow$ or the fraction of longwave irradiance form the sky, L_{sky}) as flux densities in W m^{-2} (not as radiances in W m^{-2} sr^{-1}). The symbol *L* is well established for a flux density in the urban climate and micrometeorological community (e.g. Oke, 1987), and hence we have not changed it to *M*.

→ We clarified the definition of the symbol *L* to ensure it is introduced as a flux density not a radiance. The sentence on Page 6 says new: 'The error in measuring a longwave radiation flux density (*L*)".

We still keep the term radiance where appropriate in the manuscript, but there is no need to introduce or use a symbol for it (no equations with a radiance term).

→ We introduce radiance in section 1 as "A quantification of T_0 based on remotely sensed radiance (i.e. the received longwave radiation flux *L* by sensor per unit solid angle), however, is complicated in an urban setting by three factors…"

- shortwave reflectance (p 1898, line 21): it should be replaced by "shortwave emittance". Similarly, "longwave reflectance" (p 1898, line 22) should be replaced by "longwave emittance"

→ Partially done. The term 'reflectance' has been replaced by 'reflected shortwave radiation' and 'reflected longwave radiation' depending on context (see also comment by Reviewer #1). However 'longwave emittance' (emitted radiation according to Stefan-Boltzmann) and 'longwave reflectance' (now 'reflected longwave radiation', reflection) are not the same physical process and hence the second proposed change has not been made.

The authors created a very interesting data set: urban model with facets, with reflectance / emissivity per facet. Is there a way to open this dataset to the community. As a scientist, I would be very interested in using this dataset with the DART model that I develop in order to simulate the 2 types of radiometers, using radiative transfer. The analysis of differences between the radiometer simulations and acquisitions would be useful. In addition, the possibility to simulate airborne / satellite images (UV to TIR) and LiDAR data with "DART + Data set" could be also of interest.

We appreciate the interest. We will work on a solution to host texture sheets and 3D models on a platform for future sharing and experiment documentation.

Additional changes by authors:

- Consistently use the term "thermal camera" instead of a mix of "thermal camera" and "thermal scanner"
- Fixed an error in Equation (5), where 1/(N) was missing.
- Fixed typo in title: "an urban" instead of "a urban".
- Fixed typesetting at several places (e.g. italics vs. roman for $T_{0,C}$)

Manuscript prepared for Atmos. Meas. Tech.
with version 2014/09/16 7.15 Copernicus papers of the LaTeX class copernicus.cls.
Date: 1 June 2015

The effect of radiometer placement and view on inferred directional and hemispheric radiometric temperatures of ~~a~~ an urban canopy

Christopher Adderley[1], Andreas Christen[1], and James A. Voogt[2]

[1]Department of Geography / Atmospheric Science Program, The University of British Columbia, Vancouver, BC, Canada
[2]Department of Geography, Western University, London, ON, Canada

Correspondence to: Andreas Christen (andreas.christen@ubc.ca)

Abstract.

Any radiometer at a fixed location has a biased view when observing a convoluted, three dimensional surface such as an urban canopy. The goal of this contribution is to determine the bias of various sensors views observing a simple urban residential neighbourhood (nadir, oblique, hemispherical) over a 24-hour cycle under clear weather conditions. The error in measuring ~~longwave radiance~~ a longwave radiation flux density (L) and/or inferring surface temperatures (T_0) is quantified for different times over a diurnal cycle. Panoramic time-sequential thermography (PTST) data was recorded by a thermal camera on a hydraulic mast above a residential canyon in Vancouver, BC. The dataset resolved sub-facet temperature variability of all representative urban facets in a 360° swath repetitively over a 24 hour cycle. This dataset is used along with computer graphics and vision techniques to project measured fields of L for a given time and pixel onto texture sheets of a three-dimensional urban surface model at a resolution of centimetres. The resulting dataset attributes L of each pixel on the texture sheets to different urban facets and associates facet location, azimuth, slope, material, and sky view factor. The texture sheets of L are used to calculate the complete surface temperature (~~$T_{0,C}$~~$T_{0,\mathrm{C}}$) and to simulate the ~~instantaneous~~ radiation in the field of view (~~IFOV~~FOV) of narrow and hemispheric radiometers observing the same urban surface (in absence of emissivity and atmospheric effects). The simulated directional ($T_{0,d}$) and hemispheric ($T_{0,h}$) radiometric temperatures inferred from various biased views are compared to ~~$T_{0,C}$~~$T_{0,\mathrm{C}}$. For a range of simulated off-nadir (ϕ) and azimuth (Ω) angles, $T_{0,d}(\phi,\Omega)$ and ~~$T_{0,C}$ differ between -2.7~~ $T_{0,\mathrm{C}}$ differ between -2.6 and +2.9 K over the course of the day. The effects of effective anisotropy are highest in the daytime, particularly around sunrise and sunset when different views can lead to differences in $T_{0,d}(\phi,\Omega)$ that are as high as 3.5 K. For a sensor with a narrow ~~IFOV~~ FOV in the nadir of the urban surface, $T_{0,d}(\phi=0)$ differs from ~~$T_{0,C}$ by -2.2~~ $T_{0,\mathrm{C}}$ by +1.9 K (day) and by ~~+1.6~~ -1.6 K (night).

Simulations of the ~~IFOV~~ FOV of hemispherical, downward-facing pyrgeometers at 270 positions show considerable variations in the measured L and inferred hemispherical radiometeric temperature $T_{0,h}$ as a function of both horizontal placement and height. The root mean squared error (RMSE) between different horizontal positions in retrieving outgoing longwave emittance $L_{\uparrow}$ decreased exponentially with height, and was 11.2, 6.3 and 2.0 $\mathrm{W\,m^{-2}}$ at 2, 3, and 5 times the mean building height z_b. Generally, above $3.5\,z_b$ the horizontal positional error is less than the typical accuracy of common pyrgeometers. The average $T_{0,h}$ over 24 hours determined from the hemispherical radiometer sufficiently above an urban surface is in close agreement with the average ~~$T_{0,C}$~~$T_{0,\mathrm{C}}$. However, over the course of the day, the difference between $T_{0,h}$ and ~~$T_{0,C}$~~ $T_{0,\mathrm{C}}$ shows an RMSE of ~~1.8 K (9.9~~ 1.7 K (9.4 $\mathrm{W\,m^{-2}}$) because the relative contributions of facets within the projected ~~IFOV~~ FOV of a pyrgeometer do not correspond to their fractions of the complete urban surface.

1 Introduction

The surface (or skin) temperature T_0 is a key parameter in the energy balance of land surfaces. It varies with time as a response to the radiative, conductive and convective energy transfers at the surface (Arya, 2008). The energy balance of built-up areas is altered compared to most natural vegetated land surfaces towards a higher storage of sensible heat in the fabric, a shift in the partitioning of available energy from latent to sensible heat, and the release of additional energy by anthropogenic fuel combustion and elec-

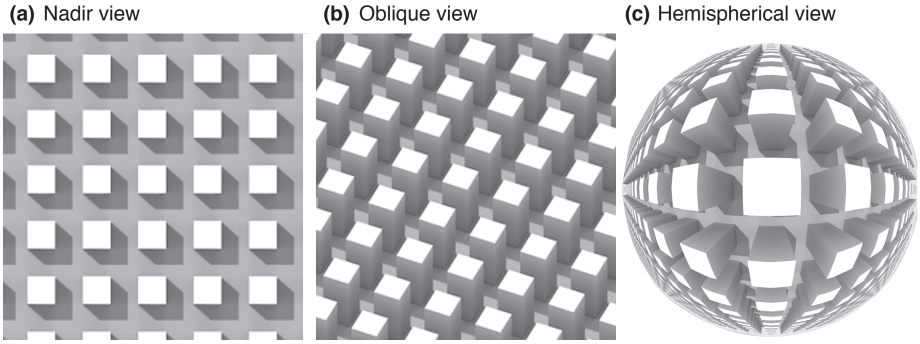

Figure 1. Projected ~~instantaneous~~ field of views (~~IFOV~~FOV) for various sensor view geometries on a generic array composed of aligned blocks of width H, height $2H$ and an inter-element spacing H. The figure shows (a) a sensor with a narrow ~~IFOV~~ FOV in the nadir, (b) a sensor with a narrow ~~IFOV~~ FOV from an oblique view point and (c) a hemispherical radiometer facing downwards.

tricity use (e.g. Oke, 1982; Cleugh and Oke, 1986; Christen and Vogt, 2004; Offerle et al., 2006). In addition, the convoluted, three-dimensional urban surface traps shortwave (solar) and longwave (terrestrial) radiation through multiple reflections (Oke, 1981; Harman et al., 2004; Krayenhoff et al., 2014). Any urban facet may receive emitted and reflected radiation from other facets comprising the urban surface. For most urban facets, the view factor of the sky ψ_{sky} is less than unity and the remainder are view factors of neighbouring urban facets (Johnson and Watson, 1984). Due to these alterations in the radiative, conductive and convective energy transfers, T_0 of urban systems is generally elevated compared to vegetated natural or agricultural surfaces in a city's surrounding. This phenomena is known as the surface urban heat island (SUHI). The SUHI is relevant to the energetics of buildings and for comfort of humans living in cities. It further establishes an altered boundary condition at the land-atmosphere interface that influences atmospheric energetics and dynamics in the urban boundary layer. This justifies our interest in retrieving T_0 of urban canopies routinely by means of ground- or satellite-based systems. Thermography ~~is generally used to convert measured radiance to~~ infers T_0 ~~by inverting the Stefann-Boltzmann Law~~using remotely measured long-wave radiation from the surface of interest. A quantification of T_0 based on remotely sensed radiance ~~in an urban setting~~(i.e. the received longwave radiation flux L by sensor per unit solid angle), however, is complicated in an urban setting by three factors:

Firstly, converting ~~measured~~ long-wave radiance to a temperature by inverting the Stefan-Boltzmann Law yields a brightness temperature T_B, which is not necessarily equal to the true surface temperature T_0. If the surface is a grey body, knowledge of the surface emissivity ε and incoming longwave radiation is required to translate T_B into T_0. The surface emissivity varies widely with materials in urban systems (Kotthaus et al., 2014) as does incoming longwave radiation on different facets as not only sky radiation, but also emittance from neighbouring facets is intercepted. Differences in emissivities in urban systems can cause differences of up to 7 K between T_B and T_0 (Voogt and Oke, 1997).

Secondly, the radiance recorded with distant sensors is affected by atmospheric effects, where absorption and re-emission of longwave radiation from gases and aerosols between sensor and ground surface will affect measured T_B (Meier et al., 2011). Generally, this affects satellite sensors to a larger extent than airborne or ground-operated sensors due to the increased path length between sensor and surface d_s. A correction requires detailed knowledge of d_s, T_a and composition of the intervening atmosphere.

Thirdly, surface temperatures of various facets $T_{0,f}$ (e.g. walls, roofs, roads) vary considerably due to differences in the facet-specific energy balance, which in turn are caused by different local solar zenith angles, shading, view factor heterogeneity, thermal/radiative surface property differences and moisture availability in an urban canopy. While the definition of T_0 of a flat and homogeneous surface is straightforward, it is more challenging to define an integrated surface temperature of a convoluted urban canopy. ~~Voogt and Oke (1997) introduced the~~ The complete surface temperature $\cancel{T_{0,C}}$ $T_{0,\mathrm{C}}$ can be approximated as the area-weighted $T_{0,f}$ of all facets that compose an urban surface. ~~To compute~~ $\cancel{T_{0,C}}$More precisely we define it here as the surface temperature calculated from the area-weighted long-wave outgoing radiation Voogt and Oke (1997) of all facets of the urban surface, which in absence of reflection ($\varepsilon = 1$) leads to:

$$T_{0,\mathrm{C}} = \sqrt[4]{\frac{\sum_f A_f T_{0,f}^4}{\sum_f A_f}} \tag{1}$$

where A_f is the surface area of any given facet f. To compute $T_{0,\mathrm{C}}$, a detailed description of all facet surface temperatures $T_{0,f}$ is required, hence $\cancel{T_{0,C}}$ $T_{0,\mathrm{C}}$ is rarely determined in detail.

Any narrow ~~IFOV~~ FOV or hemispherical radiometer located at a fixed location inherently exhibits a biased view of the 3D urban surface. Here, a narrow ~~IFOV~~ FOV sensor is defined as a pinhole camera at infinite distance ~~with a narrow instantaneous field of view (IFOV)~~ that covers a radiometric source area that is a representative patch of an urban canopy for the given off-nadir angle (ϕ) and azimuthal viewing direction (Ω). It is used to represent the view of a pixel in a satellite overpass. A hemispherical sensor is a sensor with a ~~IFOV~~ FOV of 2π with a cosine response. A typical example is the signal of a downward facing pyrgeometer. Figure 1 illustrates three typical views of a generic 'urban' array. The views correspond to the projected ~~IFOV~~ FOV of a narrow ~~IFOV~~ FOV sensor in the nadir (Figure 1a), a narrow ~~IFOV~~ FOV sensor with an oblique view direction (Figure 1b) and the view of a hemispherical radiometer facing down (Figure 1c).

Note that the view area of roofs, walls, ground and shadows is different between the three projected ~~IFOVs~~ FOVs in Figure 1. Consequently, if walls, roofs, ground and shadows have different $T_{0,f}$, the observed facet temperature of any biased view ($T_{0,d}$) integrated over its ~~IFOV~~ FOV is not necessarily equal to the simultaneously observed $T_{0,d}$ of other view directions and can also be different from ~~$T_{0,C}$~~ $T_{0,\mathrm{C}}$ (Voogt, 2008). This effect, caused by the thermal anisotropy of the canopy in combination with a biased sampling in the projected ~~IFOV~~FOV, affects airborne and satellite sensors as well as hemispherical radiometers (Voogt and Oke, 2003). Voogt and Oke (1998) found that this measurement error due to biased views combined with the thermal anisotropy of the surface exceeds that introduced by emissivity and atmospheric effects over urban surfaces (up to 10 K from anisotropy compared to 1.5 - 2.5 K and 4 - 7 K from emissivity and atmospheric effects respectively). The error becomes increasingly large as sensors deviate from the vertical, as is often the case with airborne and satellite sensors that have off-nadir viewing capabilities. Selected studies have attempted to quantify this effect (Lagouarde et al., 2004; Voogt, 2008; Lagouarde et al., 2010) for given cities using airborne measurements from different views. Nevertheless, most applications and studies simply neglect the resulting errors of radiometer placement and view direction on remotely sensed surface (brightness) temperatures of urban systems.

The goal of this contribution is to quantify the error in terms of a difference between directional radiometric temperatures ($T_{0,d}(\phi,\Omega)$) and ~~$T_{0,C}$~~ $T_{0,\mathrm{C}}$ in absence of emissivity effects, for varying ϕ and Ω of a typical urban system. A second goal is to make recommendations for the placement of hemispherical radiometers in order to best capture 'representative' upwelling longwave radiation.

2 Methods

The proposed method uses panoramic time sequential thermography (PTST) data (Section 2.1) and a digital urban surface model (Section 2.2) to reconstruct $T_{0,f}$ over time of all relevant urban facets (Section 2.3). This dataset is then used to calculate ~~$T_{0,C}$~~ $T_{0,\mathrm{C}}$ of the convoluted urban canopy and to simulate biased views of narrow ~~IFOV~~ FOV radiometers and hemispheric radiometers using computer graphics methods (Section 2.4). Based on $T_{0,f}$, emittance is simulated and the receipt of radiation is modelled for various biased views at different locations.

2.1 Panoramic time sequential thermography

2.1.1 Site

The PTST data was obtained from a thermal camera on top of a mobile hydraulic mast installed in a relatively uniform suburban area (Sunset neighbourhood) of Vancouver, BC, Canada. This area has various long-term instrumentation for urban climate monitoring in place, including measurements of radiative and convective fluxes on top of a 26 m long-term flux tower named 'Vancouver-Sunset' (Christen et al., 2013). The area is characterized by detached houses (Local Climate Zone 6, Stewart and Oke (2012)) following an orthogonal street grid layout. Measurements and modelling took place is the 6100 block of Elgin Street between E 45$^{\mathrm{th}}$ and E 46$^{\mathrm{th}}$ Ave ($49°13'42''\mathrm{N}, 123°05'02''\mathrm{N}$, WGS-84), located 500 m to the NW of the 'Vancouver-Sunset' flux tower. The selected canyon section has a total of 12 buildings uniformly aligned along a north-south road, which minimizes asymmetric solar irradiance interactions over the course of a day. The lack of tall vegetation in the canyon section simplifies the projection of measured longwave emittance from the PTST dataset on to a urban surface model (USM) and reduces the geometric complexity and uncertainties associated with the movement of trees in wind. The canyon section studied had a canyon width of 33.3 m. A concrete road of 13 m width was located roughly in the centre of the canyon bounded with ~~symmetric~~ lawns (and sidewalks) ~~of 10 m~~ on both sides. ~~Most of the houses~~ Houses in the canyon were all built between 1971 and 1976 and are of similar dimensions and materials, with a rectangular footprint oriented perpendicular to the street and low-pitched roofs with slopes from 10° to 15°. Building peak heights vary from 6.2 to 7.1 m in a two-floor configuration, with an area-averaged roof area height of 6.23 m. Total building volumes range from 520 to 750 m^3. Most buildings have extensive back porches often with a carport towards a 6 m wide back lane (asphalt, concrete and bare soil). The relative uniformity of the structures simplified the complex geometry and proved helpful when statistically filling obstructed areas. The model domain encompassed a west-east (cross-canyon) extent of 90 m and a North-South (along-canyon) extent of 92 m (Figure 3).

2.1.2 Instrumentation

A pan and tilt device allowed the camera to record 360° scans at different tilt angles over the course of a 24-hour cycle at

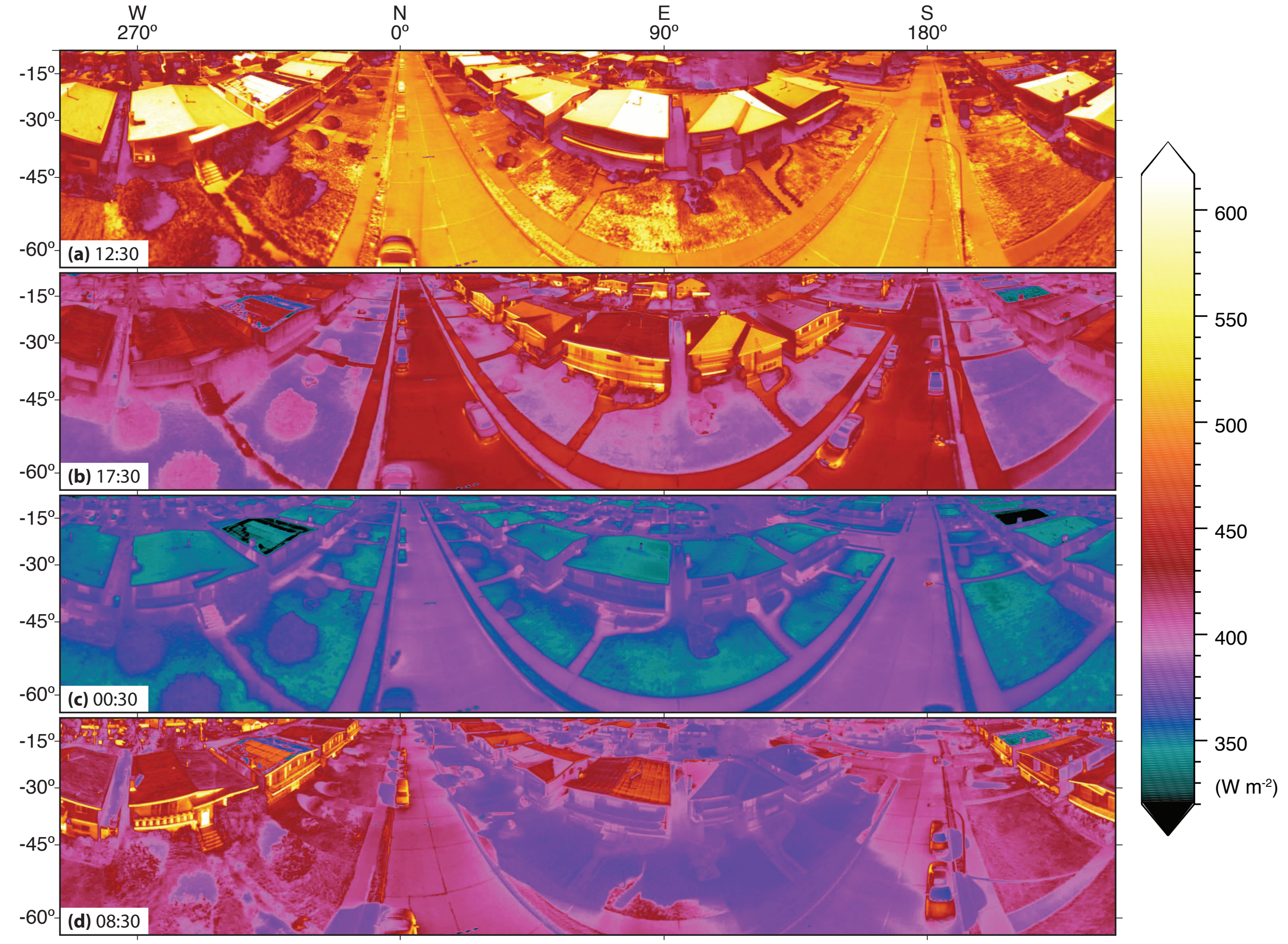

Figure 2. Selected time steps of the panoramic time sequential thermography (PTST) dataset for September 14, 2008, 12:30 (a), 17:30 (b) and September 15, 2008, 00:30 and 08:30. Each panorama is composed of ≈120 single images and projected using a conformal Mercator grid relative to the local horizon. See web supplement for PTST data from additional time steps.

a temporal resolution of 60 min. The field of view (FOV) of the PTST dataset corresponds roughly to that of a ~~to a~~ downward-facing hemispherical radiometer. In contrast to a radiometer that returns a single, integrated value over time, the spatially resolving PTST covers the lower hemisphere with $> 4 \times 10^4$ pixels over time (Figure 2).

A Thermovision A40M thermal infrared camera (FLIR Systems, Wilsonville, Oregon, USA) with a wide angle lens was mounted atop a mobile hydraulic mast in the centre of the canyon studied at a height of 17.95 m above ground level (2.88 z_b). The system has ~~an IFOV~~ a FOV of $61° \times 48°$ corresponding to 320 by 240 pixels. Every hour, the ~~scanner~~ camera was rotated in a 360° panorama at two different tilt angles, one at approximately 65° off-nadir, another at approximately 45° resulting in panoramic scans with a spatial resolution of 1.07×10^{-5} sr, which corresponds to panoramas of > 40M pixels per scan. The panorama omitted a cone directly in the nadir, where the mast was located. Details of the scan pattern can be found in Adderley (2012).

The Thermovision A40M uses an uncooled microbolometer sensor to retrieve T_B from measurements of incoming longwave radiation. The microbolometer is sensitive to thermal infrared radiation between 7.5 to 15 μm although highest sensitivity is concentrated between ~~8 and 13~~ 9.2 and 11.8 μm (> 90% sensitive). The detectors have a radiometric resolution of 16 bits/pixel. At ambient T_0 near 300 K, a sensitivity of 0.08 K is achievable, with an absolute accuracy of ± 2 K (Flir Systems, 2004). Data from the thermal camera was recorded in digital format via FireWire on a PC. Each panoramic scan resulted in 250 frames at 320 by 240 pixels.

Two tripods with meteorological sensors were deployed to the north of the hydraulic mast on lawns to the east and west of the street and provided measurements of air temperature T_a and relative humidity RH at 0.3 m (HMP-35, Campbell Scientific Inc., Logan, UT, USA).

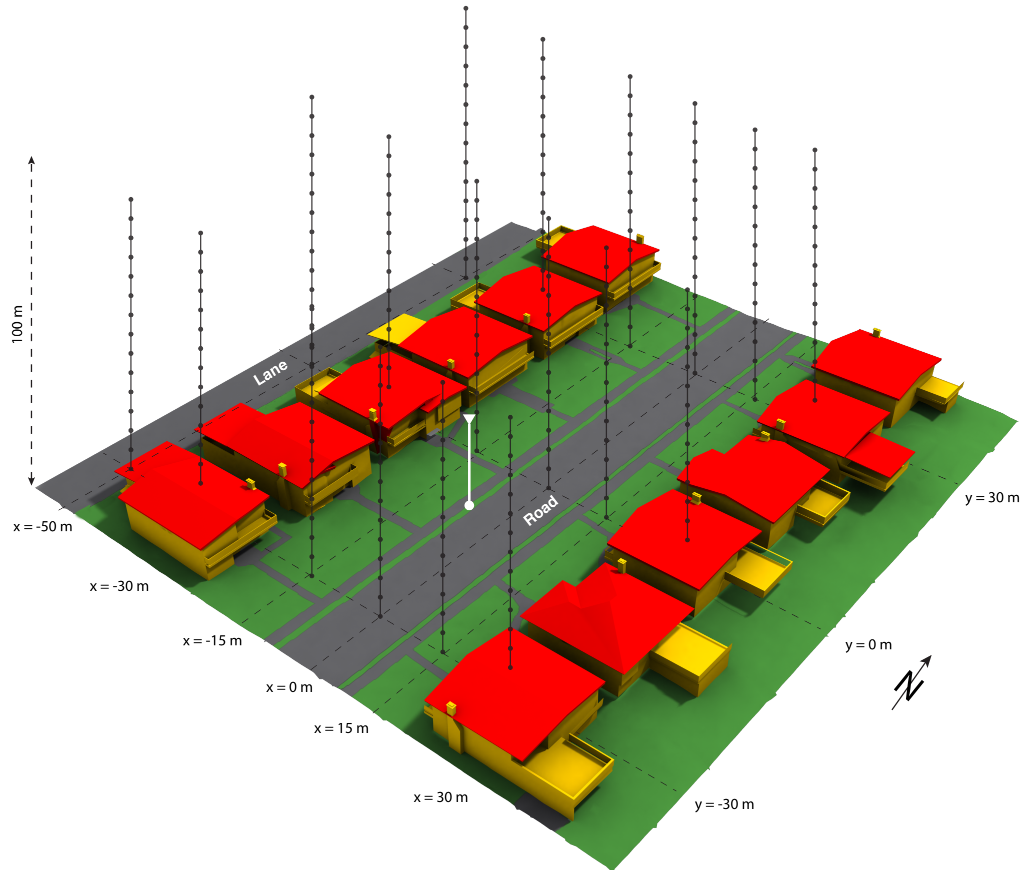

Figure 3. Rendering of the modelled urban canyon with facet classifications (roofs: red, walls and other building structures: yellow, lawns: green, roads and pathways: grey), location of the hydraulic mast (white line) and the thermal camera (white triangle). The vertical black dots refer to the 270 simulated positions of hemispherical radiometer locations (see Section 3.3)

Those were used for atmospheric correction (see Section 2.3). Additionally, at 'Vancouver Sunset' (49°13′34″N 123°04′42″W, WGS-84), a CNR1 4-Component Radiometer (Kipp and Zonen, Delft, Netherlands) provided measurements of ~~shortwave~~ hemispherical radiation fluxes at 26 m above the surface. Shortwave irradiance ($K_{\downarrow}$), ~~shortwave reflectance~~ and reflected shortwave radiation ($K_{\uparrow}$) ~~,~~ were measured using two CM3 pyranometers, and longwave irradiance ($L_{\downarrow}$), and ~~longwave emittance and reflectance~~ the sum of emitted and reflected longwave radiation ($L_{\uparrow}$) ~~at 26 m above the urban surface~~were quantified using two CG3 pyrgeometers (spectral sensitivity from 5 to 50 μm), all at 5 min temporal resolution.

2.1.3 Study period

Observations were made between 14 September 2008, 13:30 and 15 September, 2008, 12:30 and resulted in one panoramic scan every 30 minutes of which every other run was used in this study. The weather during the field campaign was cloud-free. A cloud free situation with direct-beam irradiance maximizes thermal anisotropy and is usually the situation when thermal remote sensing is performed. During the study period, air temperatures ranged between 284.7 K and 298.5 K in the canyon. Daily total measured $K_{\downarrow}$ was 31.9 $\mathrm{MJ\,m^{-2}\,day^{-1}}$, of which 4.9 $\mathrm{MJ\,m^{-2}\,day^{-1}}$ was reflected ($K_{\uparrow}$). Daily total measured $L_{\downarrow}$ was 29.4 $\mathrm{MJ\,m^{-2}\,day^{-1}}$, and $L_{\uparrow}$ was 37.1 $\mathrm{MJ\,m^{-2}\,day^{-1}}$.

2.2 Urban surface model

A highly-detailed 3D urban surface model (USM) of the urban surface was constructed based on detailed surveying data.

2.2.1 Geometric information

Basic positional information of the urban surface was collected with a Trimble R7 differential GPS (DGPS) unit (Trimble, Sunnyvale, California, USA), with horizontal position accuracy < 1 cm and vertical accuracy < 2 cm. The DGPS data was supplemented with Light Detection and Ranging (LiDAR) data flown during March 2007 by a fixed wing aircraft operating a TRSI Mark II discrete-return sensor (Goodwin et al., 2009). For the purposes of this project, only the ground returns of the LiDAR were used. Close-range photogrammetry was chosen to reconstruct buildings. In close-range photogrammetry, multiple images from varying directions of the same building are correlated to solve 3D positions of points and lines. These features are then assembled into vector representations of buildings. The images collected for photogrammetry were taken at ground level and from atop the same hydraulic mast at multiple locations using a Nikon D100 digital single-lens-reflex (SLR) camera (Nikon, Tokyo, Japan), equipped with a 28 mm Nikkor lens. Eos Photomodeler (Version 6.2, Eos Systems, Vancouver, BC, Canada) was used to reconstruct vector building models from digital SLR images. Eos Photomodeler has been used previously for modeling of urban form with good performance (Nikiforiadis and Pitts, 2003). The street canyon was broken down into its component features, with each house being modelled individually, and then integrated together in 3D Studio Max (Version 8, Autodesk, San Raphael, CA, USA) to form a complete canyon 3D model. The resulting USM is visualized in Figure 3 in form of a 3D projection.

2.2.2 Facet and material information

The material type defines the emissivity ε of a facet ~~(?)~~ (Oke, 1987) and other underlying material properties (e.g. thermal admittance). A survey of the ground-level photos and orthophotography was undertaken, creating an inventory of all material types in the canyon (Table 1). Materials were manually marked on the triangles composing the USM using a material identifier code. Where material boundaries did not fit the topology of the model, additional triangles were added in order to correctly attribute materials. To each of the materials, a ε value was attributed based on Flir Systems (2004). It was assumed that ε is isotropic, i.e. surfaces show a Lambertian behavior in the long-wave band. Also aging and weathering of surfaces was not considered in the attribution of ε to materials.

2.2.3 Sky view factor

The sky view factor (ψ_{sky}) was calculated for each surface pixel using an ambient occlusion algorithm in 3D Studio Max. In ambient occlusion, each pixel on a 3D model is the source for a Monte Carlo raycasting simulation, where sampling rays are cast in all directions from the pixel with a cosine probability relative to the zenith. To test the ability of ambient occlusion algorithms to numerically determining ψ_{sky} in complex geometries, several idealized 3D situations in which ψ_{sky} was known were compared against this algorithm. The results showed good correspondence with a maximum error in ψ_{sky} of 0.02, indicating that the ambient occlusion method was adequate (Adderley, 2012).

Table 1. Inventory of materials found in the Elgin Street canyon with attributed emissivities (Flir Systems, 2004), and relative frequency in % of complete surface.

Material	Emissivity ε	Fraction of complete surface (%)		
		Roofs	Walls	Ground
Aluminum	0.70	6.9	0.6	0.0
Asphalt / tar	0.97	7.4	0.0	0.0
Brick	0.93	0.0	0.9	0.0
Concrete	0.92	0.0	0.1	9.4
Glass window	0.80	0.0	3.0	0.0
Grass	0.95	0.0	0.0	49.9
Paint	0.93	0.7	18.6	0.0
Rock	0.82	0.0	0.4	0.0
Stucco	0.91	0.0	2.0	0.0
All		15.1	25.6	59.2

2.3 Projecting measured T_B on surface

Using coordinate transformation, measured T_B from each frame pixel in the PTST data was projected on the USM. ~~''~~As a first step, the three-dimensional vector-based USM was decomposed into planar bitmap images by assigning a set of planar 2D coordinates to each face of the model (UVW mapping, Shirley et al., 2009). Cartesian coordinates of all pixels (x_s, y_s, z_s) were translated to global spherical coordinates where θ_s and ω_s are the spherical tilt and azimuth angles of a pixel relative to the camera location, and d_s is the distance of that pixel to the camera ~~at~~ location. Texture maps of θ_s, ω_s and d_s were also stored for all building and ground objects. Then each thermal camera frame pixel was interactively projected onto the 3D USM, using a search algorithm that matched θ_s and ω_s of the PTST dataset to θ_s and ω_s of the USM. Manual inspection of projected panoramas revealed some areas of incorrect attribution along edges and on distant objects. Those areas were eliminated manually and filled using a gap-filling algorithm. Details of this procedure are described in Adderley (2012)

2.3.1 Atmospheric correction

Atmospheric correction ~~was~~ were performed for each time step after projecting ~~T_B~~ T_B back onto the USM. A set of MODTRAN simulations were run for the current camera spectral range following the procedure outlined in Meier et al. (2011). These corrections ~~are based on each pixels~~ considered path length (d_s), ~~and~~ local air temperature (T_a ~~and RH measured simultaneously in the canyon~~, measured in canyon), sensor measured brightness temperature T_B and relative humidity RH (measured in canyon). Due to the large number of T_a, T_B and path length values, it was impractical to run a MODTRAN simulation for each combination. Instead, a number of scenarios were run by changing T_B

at 5 K intervals (for range 278 - 323 K), T_a in 2 K intervals (273 - 303 K), RH at 2% intervals (40 - 80%), and d at intervals of 10 m (15 - 75 m). The resulting look-up table was interpolated linearly ~~for the actual values~~ between two T_B values to match the actual T_B of each pixel, while for all other parameters the nearest value was used. Corrections of individual pixels ranged between 0.7 and 8.6 K (road, midday, large d_s) over the 24 h.

2.3.2 Emissivity correction

To retrieve each pixel's $T_{0,px}$ from measured $T_{B,px}$ ~~the following equation was solved:~~ we used the broad-band equation showing that longwave flux density $L_{\uparrow,px}$ observed from a surface is the sum of emittance and long-wave reflected radiation (Oke, 1987) :

$$L_{\uparrow,px} = \sigma T_{B,px}^4 = \varepsilon_{px}\sigma T_{0,px}^4 + (1-\varepsilon_{px})L_{\downarrow,px} \tag{2}$$

ε_{px} is the pixel's emissivity previously attributed based on material. Equation 2 was then solved for $T_{0,px}$:

$$T_{0,px} = \sqrt[4]{\frac{\sigma T_{B,px} - (1-\varepsilon_{px})L_{\downarrow,px}}{\sigma\varepsilon_{px}}} \tag{3}$$

A pixel's incoming longwave radiation $L_{\downarrow,px}$ is approximated as the sum of longwave radiation from the sky weighted by the pixel's sky view factor (ψ_{sky}), and the longwave radiation from the canyon, weighted by the pixel' ground view factor (1 - ψ_{sky})~~:~~.

$$L_{\downarrow} = \psi_{\mathrm{sky}}L_{\mathrm{sky}} + (1-\psi_{\mathrm{sky}})\sigma T_{0,\mathrm{C}}^4 \tag{4}$$

L_{sky} is the directly measured incoming broad-band longwave radiation at the tower 'Vancouver Sunset' for the given time step. The approximation in Eq. 4 assumes that atmospheric irradiance is isotropic, and that the surrounding urban facets all have a uniform surface temperature equal to $T_{0,\mathrm{C}}$. In this equation we first approximate $T_{0,\mathrm{C}}$ by ~~$T_{B,C}$~~ $T_{\mathrm{B,C}}$. The correction was iteratively applied as the temperature correction changes the value of $T_{0,\mathrm{C}}$. This correction was performed repeatedly until the corrected surface temperature $T_{0,px}$ for one iteration was not significantly different from $T_{0,px}$ for the previous iteration (difference of less than 0.25 K). This was accomplished within 5 iterations.

2.3.3 Obstructed surfaces

As the thermal ~~scanner~~ camera is at a fixed location, it is evident that not all pixels in the texture maps can be seen by the camera. ~~Naturally, the~~ Secondly selected areas were removed by manual inspection, because of minor misalignments along edges. The mean visibility of roofs and ground in the entire domain are 95% and 72%, respectively. The visibility of E-W walls is only 46% (lane-facing walls of buildings cannot be seen). For N-S walls, the visibility is good in the four nearest houses ($\approx 90\%$), however it is very poor ($< 10\%$) for all houses further away from the thermal camera. Hence, the PTST dataset is also a preferred view, however its panoramic nature means that it contains data from all relevant facets of the urban canopy. However for simulating alternative projected ~~IFOVs~~ FOVs the USM needs to be populated on all sides with temperatures.

The gap filling of unseen pixels was based on an adaptive search algorithm. For each pixel requiring interpolation, four predictors were extracted: the pixel facet type (roof, wall, ground), pixel material type, pixel orientation (azimuth and slope) and pixel ψ_{sky}. Each of these factors affects T_B of a surface. A search algorithm then looked at all measured pixels in the same texture sheet that matched the features to those belonging to the pixel to be filled. Matched pixels had to have identical facet type and material to the originating pixel. Sky view factor and orientation had variable thresholds: the orientation threshold was based on the slope of the pixel. Pixels with a high slope required an orientation value that was very close (within 5°), while pixels with a low slope had a more relaxed threshold (within 15°). The ~~threshold for~~ pixels used to statistically fill the obstructed target pixel had to experience a difference in ψ_{sky} ~~factor was~~ of less than 0.03.

If a similar pixel could not be found on the same object (i.e. house), the sheets for all other houses and the ground were examined. This was key in areas where only one side of the house was visible to the thermal ~~scanner~~image, as pixels for the opposite side would all be unattributed. This gap filling assumes that the houses have similar thermal behaviour in each direction from the tower. The same wall orientation is visible on the other side of the ~~scanner~~ scanning camera (i.e. panorama) and houses with pixels matching the orientation could be always found. If a similar pixel was still not found, the ψ_{sky} and orientation thresholds were relaxed by 5%, and the search was repeated. In this way all pixels were matched.

2.4 Simulating the view of different radiometers

In order to examine the effect of biased view directions, the corrected surface temperature of each pixel ($T_{0,px}$) encoded in UVW texture form was first translated to a longwave emittance from the pixel ($L_{px} = \sigma T_{0,px}^4$), removing any emissivity effects in the simulation. Sensors were rendered using different angles and camera models using raytracing simulations in 3D Studio Max. Two sensor types were rendered: a simulation of a narrow ~~IFOV~~ FOV sensor representing a typical airborne or satellite radiometer (Section 2.4.2) and a simulation of a hemispherical downward-facing pyrgeometer with ~~an IFOV~~ a FOV of 2π (Section 2.4.3). Atmospheric effects of intervening gases and aerosols were not considered in the simulations of the sensors. This way, any differences of biased views are solely caused by geometric effects in the absence of emissivity and atmospheric effects.

To represent L_{px} at sufficient resolution, texture maps of 32-bit truecolor images were generated for the three dimensional surface and imported into 3D Studio Max. This was necessary as the number of data values exceeds the range available using a traditional 8-bit greyscale map (256). With a 32 bit red, green, blue and transparency (RGBA) image, the number of possible data values is extended to $> 4 \times 10^9$, which is easily sufficient for representing flux densities at the thermal camera data-depth. The number of unique L_{px} values present in the entire street canyon for a given timestep were counted, sorted by magnitude, and indexed, with each value assigned a RGBA value. An image was created by matching the RGBA values to the L_{px} values for each map and exported into portable network graphics (PNG) images for each timestep along with indexing data containing the transformation from L_{px} to colours. These PNG images were then imported and assigned to the correct ~~models~~ facets of the 3D ~~model~~ USM in 3D Studio Max. This converted the ~~model~~thermal data, split by texture maps, into a 3D polygonal structure which could interact with the software's lighting and raytracing engines for view direction simulations.

All rendered visual quality enhancements in 3D Studio Max were disabled in order to avoid any filtering. Each sensor's projected ~~IFOV~~ FOV was rendered to a single frame 256 × 256 pixel array of RGBA values and exported to a PNG image. This was determined a high enough resolution to render truthfully all relevant facets of the urban surface even for sensors at the highest locations. The RGBA values were converted to pixel longwave values L_{px} through the use of the original lookup table. The 256×256 matrix of converted $L_{px}(x, y)$ values was then averaged to a single value of L_{px}. The scalar L_{px} was then converted to a black body surface temperature of the biased view, $T_{0,d}$, simulating the physical procedure when retrieving surface temperatures.

2.4.1 Cyclic domain

If a simulation of a sensor at a high altitude is desired, the single domain of 92 m by 90 m is insufficient. The domain was therefore repeated in the x and y directions, to create an effectively infinite suburban residential area conserving the anisotropy of the measured area. The resulting domain was then repeated approximately 50 times in both horizontal directions (45,000 houses). Though not completely infinite, it approximates an infinite plane for the view directions as simulated for a hemispherical downwards-facing sensor. The tiled surface is not completely representative of a city: it has no east-west streets, but serves adequately as an idealized suburban surface with the given dataset. The characteristics of the cyclic domain are summarized in Table 2.

2.4.2 Narrow ~~IFOV~~ FOV rendering

In 3D Studio Max, a pinhole-type camera was placed facing downward at 10^4 m above the tiled surface. A ~~IFOV~~ FOV of 1° was used for the camera with rendered pixel dimensions of 256 by 256 pixels (Figure 4a). These parameters approx-

Table 2. Morphometric parameters describing the simulated urban domain.

	Description	Value
z_b	Area-weighted building height	$6.23\,\mathrm{m}$
V_b	Building volume per domain area	$2.65\,\mathrm{m^3\,m^{-2}}$
x_c	Characteristic street canyon width	$33.3\,\mathrm{m}$
y_c	Characteristic along-canyon inter-building spacing	$3.23\,\mathrm{m}$
λ_s	Street canyon aspect ratio (z_b/x_c)	0.18
λ_b	Plan area ratio of buildings	$0.34\,\mathrm{m^2\,m^{-2}}$
λ_i	Plan area ratio of impervious ground	$0.21\,\mathrm{m^2\,m^{-2}}$
λ_v	Plan area ratio of vegetation	$0.55\,\mathrm{m^2\,m^{-2}}$
λ_c	Complete aspect ratio	$3.61\,\mathrm{m^2\,m^{-2}}$

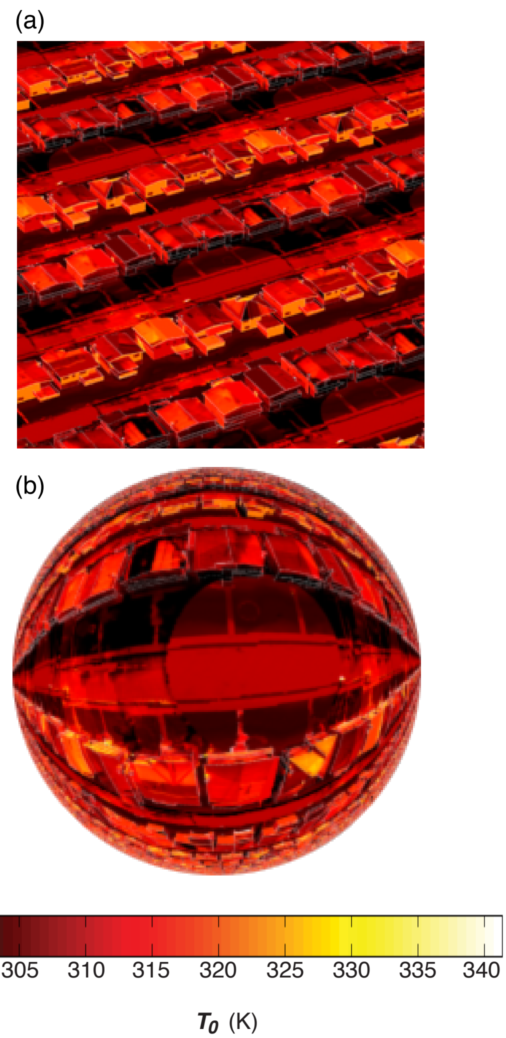

Figure 4. Examples of rendered (a) narrow ~~IFOV~~ FOV and (b) hemispherical radiometer rendering at 13:30.

imate a sensor pointing down at nadir with ~~an instantaneous projected IFOV~~ a projected FOV of 30 m. For oblique views, the camera was angled so that each frame faced the same centre point of the tiled surface (but the projected ~~IFOV~~ FOV was larger). ~~Camera-centre image azimuths (α_i~~Camera azimuths (Ω) from 0° to 360° at an interval of 30° were simulated with ~~image~~ off-nadir angles (~~β_i) of~~ ϕ) from 0° to 70° at intervals of 10°. This resulted in a total of 96 different view simulations for each of the 24 hourly steps.

2.4.3 Hemispherical sensor rendering

Hemispherical sensors were rendered as circular areas with diameter 256 pixels (Figure 4b). The sensor was positioned directly above several points in three different transects from west to east throughout the canyon. For each position, varying heights were chosen (Figure 3), from 2 m to 10 m (at 2 m intervals) and from 10 m to 100 m at 4 m intervals (up to approximately z/z_b = 10). A total of 270 hemispherical radiometer positions were rendered for a total of four timesteps (13:30, 18:30, 00:30, and 06:30). These 6-hour intervals gave a reasonable assessment of the canyon temperature patterns over time for the available computational time. The imported $L_{px,h}$ was then corrected for angle-of-incidence effects (cosine response) and averaged to recover a single signal of L_h for each radiometer position. Similar to the narrow FOV sensors, the simulated hemispherical sensor signals consider only emittance, and treat the surface as a black body. Note that measured L_h from a real broad-band pyrgeometer at different heights would additionally be impacted by atmospheric effects between the surface and the measurement level that are not considered in the current study.

3 Results and discussion

3.1 Complete surface temperature

Area-weighted $T_{0,f}$ for different facet types are calculated by weighting corrected surface temperatures of each pixel i in the texture sheets ~~$T_{0,px}$~~ $T_{0,px,i}$ with by their pixel area ~~A_{px}:~~ $A_{px,i}$:

$$T_{0,f} = \frac{1}{I\,N\,A_T}\sum_i I_{f,i}\,A_{px,i}T_{0,px,i} \qquad (5)$$

where A_T is the complete total area of the 3D model, N is the total number of pixels, and $I_{f,i}$ is an indicator function which is equal one if the pixel is attributed to facet type f and zero otherwise. ~~Similarly, $T_{0,C}$ was calculated as $T_{0,C}$, and~~ I is the fraction of A_T that is attributed to facet type f (see Tab. 1).

To ensure a consistent comparison between $T_{0,\mathrm{C}}$ and simulated radiometer data averaged over the FOV of the instrument under study, $T_{0,\mathrm{C}}$ was calculated for each time step from each pixel's $T_{0,px,i}$ converted to a long-wave emittance, and then averaging the long-wave emittance and converting back to a brightness temperature, following Eq. 1:

$$T_{0,\mathrm{C}} = \sqrt[4]{\frac{1}{N A_T}\sum_i A_{px,i}T^4_{0,px,i}} \qquad (6)$$

$T_{0,\mathrm{C}}$, and $T_{0,f}$ of walls, roofs and ground are shown over the 24 hour cycle in Figure 5.

$T_{0,f}$ of roofs display a distinct trend of higher values in the daytime with a spatial mean of 320.8 K (standard deviation ± 9.1 K) at 13:30, cooling down to lowest temperatures at night with a spatial mean of 280.8 K (± 2.5 K) at 06:30. Roofs will receive the most shortwave irradiance by day due to the lack of shading, and will cool rapidly by longwave emission at night due to their high ψ_{sky} and limited heat storage capabilities. Roof temperatures hence show the largest diurnal amplitude of 40 K (Table 3), which is in the typical range of reported values for clear-sky days in other studies (Masson et al., 2002; Chudnovsky et al., 2004; Christen et al., 2012; Sal

$T_{0,f}$ of the ground facet shows the ~~opposite behaviour~~smallest diurnal range, with lowest $T_{0,f}$ of all facet classes during the day with a maximum spatial mean of 311.5 K (± 3.35 K) at 14:30 and highest mean minimum $T_{0,f}$ of all facets at night with 286.4 K (± 1.7 K) at 06:30. In-class variation is more limited than the roofs and is more constant over the entire dataset, with minimal decrease at night. The ground facet has distinct material differences from roofs, being composed of 16% concrete (road) and 84% grass. Grass will not heat up as much by day due to transpirative cooling and consequently be cooled less at night. There was large spatial variability of grass temperatures due to different moisture availability

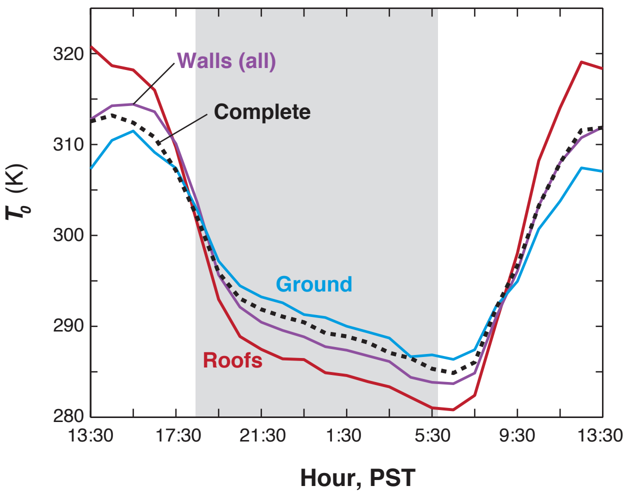

Figure 5. Area-weighted average $T_{0,f}$ over the course of the field observations along with complete surface temperature ~~$T_{0,C}$~~$T_{0,\mathrm{C}}$. The shaded area is nighttime.

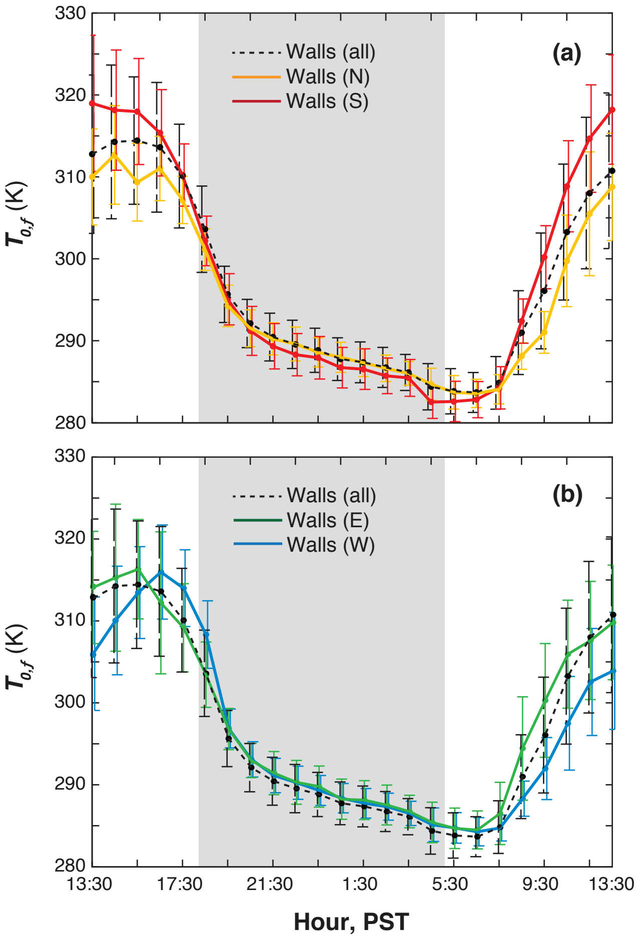

Figure 6. Area-weighted wall temperatures divided by facet orientation. Error bars show one standard deviation. (a) North and South facing walls. (b) East and West facing walls.

(irrigation). For the road, we see warmer $T_{0,f}$ at night in the canyon floor compared to roofs. The road tends to have an intermediate $\psi_{\rm sky}$ due to its location in the centre of the canyon and the receipt of longwave radiation from nearby walls will retard cooling in the canyon floor, compared to roof tops.

Walls exhibit a $T_{0,f}$ between ground and roofs ~~in Figure 7~~ (Fig. 5) with a spatially averaged maximum of 314.4 K (± 7.8 K) at 14:30 and a minimum of 283.7 K (± 2.4 K) at 06:30. Figure 6 shows $T_{0,f}$ split by facet orientation into four cardinal directions. Notably, south facing walls achieve warmer 24 hour temperatures of 298.5 K (± 4.0 K) than others due to their sun-facing aspect. ~~Interestingly, they achieve cooler temperatures at night.~~ At night, north and south facing walls are slightly colder than west and east facing walls (Tab. 3). This can be explained by the substantial roof overhangs and balconies, that reduce the local sky view faction over the west and east facing walls and possibly the fact that east and west facing walls have more windows. Excluding the night-time situation, the north-facing walls are cooler than the south-facing walls by an average of 5.6 K (± 3.6 K), which is to be expected considering the location of the sun at this time of the year. North-facing walls are only irradiated for < 30 min near sunrise and sunset in cases where the solar altitude is < 3.9° (substantial shading is expected). In summary, walls experience intermediate $T_{0,f}$. During day $T_{0,f}$ is highest for roofs, followed by walls and lowest for the ground. During night $T_{0,f}$ is highest for ground, followed by walls and lowest for roofs.

Table 3 separates the behaviour of canyon facets by type, material and orientation. In general, it is expected that the mean diurnal amplitude of $T_{0,f}$ should be inversely related to the thermal admittance μ of the facet in question: low μ result in larger mean diurnal amplitudes. Roofs have lowest μ due to primarily low conductivities. Ground facets have reasonably high μ and reflect this in a low mean diurnal amplitude (25.1 K). The effect of orientation is evident for walls. North-facing walls having the lowest mean diurnal amplitude (29.1 K). The largest variation (south facing) shows the highest diurnal amplitude (36.5 K), and the east and west facing walls, which also have large variations in shading, show identical mean diurnal amplitudes (31.7 K).

3.2 Narrow ~~IFOV~~ FOV radiometers

3.2.1 Nadir view

Figure 7 compares the surface temperature inferred from a narrow ~~IFOV~~ FOV sensor at nadir ($T_{0,d}(\phi=0)$) to ~~$T_{0,C}$: $T_{0,C}$~~ $T_{0,C}$. $T_{0,C}$ is lower than $T_{0,d}(\phi=0)$ in the daytime and is higher following sunset in a situation that favours strong radiative cooling (many facets with high $\psi_{\rm sky}$, clear skies, both of which are present in this situation). The largest difference is present near solar noon (solar altitude 43°); at this ~~point a sensor with a narrow IFOV in the nadir sees mostly horizontal facets, roofs and ground facets, which tend to be warmer due to material differences than $T_{0,C}$ which also includes walls~~time horizontal surfaces, especially those with large $\psi_{\rm sky}$, are warm relative to vertical surfaces and dominate the radiance received by a narrow FOV sensor. The reverse is true at night, where wall $T_{0,f}$ are likely to be higher (see Figure 5) than $T_{0,f}$ of horizontal facets, in particular those of roofs, due to their low thermal admittance.

A maximum difference $T_{0,d}(\phi=0)-T_{0,C}$ of +~~2.2~~ 2.0 K is observed at 13:30 (overestimation by the sensor), and values are closest at 10:30. Over the course of the day, the root mean squared error (RMSE) of $T_{0,d}(\phi=0)-T_{0,C}$ is 1.2 K. Roberts (2010) compared ~~$T_{0,C}$~~ $T_{0,C}$ to $T_{0,d}(\phi=0)$ of a hardware scale model over the course of a day. The maximum overestimation $T_{0,d}(\phi=0)-T_{0,C}$ is reported at solar noon and has a value of around +2.5 K, which is similar to this study (+2.2 K). During nighttime, the $T_{0,d}(\phi=0)-T_{0,C}$ differences for the lowest density configuration in Roberts (2010) ~~ranges~~ range between -0.5 and -1 K, which is again

Table 3. Summarized area-weighted mean maximum and minimum surface temperatures with calculated mean diurnal amplitude for canyon materials, divided by facet type and orientation. Values in brackets show standard deviations.

Facet type	Mean maximum temperature (K)	Mean minimum temperature (K)	Mean diurnal amplitude (K)
Roofs (all)	320.8 (± 9.1)	280.8 (± 2.5)	40.0
asphalt only	321.0 (± 6.2)	280.9 (± 1.8)	40.1
metal only	294.8 (± 10.9)	257.5 (± 2.3)	37.3
Ground (all)	311.5 (± 3.4)	286.4 (± 1.7)	25.1
grass only	309.3 (± 3.1)	284.6 (± 2.0)	24.7
concrete	317.6 (± 3.1)	287.8 (± 1.6)	29.8
Walls (all)	314.4 (± 7.8)	283.7 (± 2.4)	30.7
North-facing walls	312.7 (± 6.0)	283.6 (± 1.7)	29.1
South-facing walls	319.0 (± 8.3)	282.5 (± 2.0)	36.5
East-facing walls	316.3 (± 6.0)	284.6 (± 2.3)	31.7
West-facing walls	316.0 (± 5.7)	284.3 (± 1.7)	31.7

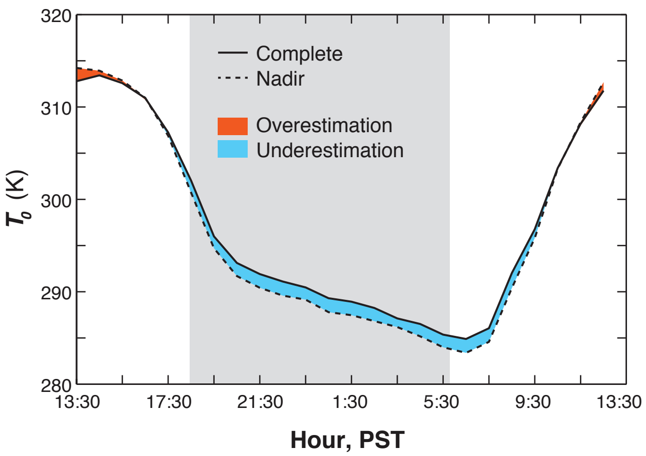

Figure 7. Diurnal course of ~~$T_{0,C}$~~ $T_{0,\mathrm{C}}$ compared to $T_{0,d}(\phi = 0)$ of a sensor with a narrow ~~IFOV~~ FOV in the nadir.

comparable to values found here (-0.9 to ~~-1.5~~ -1.4 K, underestimation).

3.2.2 Oblique view

The large number of view directions simulated allows the systematic examination of the difference between directional and complete surface temperatures for oblique sensor views. The difference $T_{0,d} - T_{0,C}$ is plotted in polar form in Figure 8. In these polar plots, each pixel represents a temperature value for a view direction as plotted by the off-nadir angle (ϕ) and azimuth from geographic north (Ω) of the sensor location. At the centre of the plot lies the value at nadir ($\phi = 0$).

In the daytime situations, the effects of anisotropy are clearly visible, particularly before solar noon (Figure 8b). Here in half of the hemisphere, $T_{0,d}$ ~~overestimates $T_{0,C}$~~ underestimates $T_{0,\mathrm{C}}$ (opposed to solar position) and in the other half $T_{0,d}$ ~~underestimates $T_{0,C}$~~ overestimates $T_{0,\mathrm{C}}$ (same side as solar position - the solar position is represented by a cross in 8b). Generally over the day, the hotspot of highest $T_{0,d}$ is following the solar position (see also web-supplement). When the position of the sun is close to the direction of the sensor, the signal is mostly overestimated. The daytime hotspot has a slight lag from the sun's position (approximately 1 hour).

This pattern of higher visible $T_{0,d}$ from the direction of the sun persists until the sun moves below the horizon (by 17:30) at which point the difference between west and eastern facets begins to be reduced, but is still sustained a few hours (Figure 8, right). By 18:30, most modeled views show a $T_{0,d}$ lower than ~~$T_{0,C}$~~ $T_{0,\mathrm{C}}$. The south facing regions remains warm due to residual heat stored that is now released.

Moving into the nighttime, a continued decay of the daytime hotspot is evident until 21:30 (see web supplement). Until this point, views from the south continue to be consistently warmer, underestimating ~~$T_{0,C}$~~ $T_{0,\mathrm{C}}$ by only 0.5~~-1.0~~ -1.1 K. For most other views, there is a consistent underestimation of ~~$T_{0,C}$~~ $T_{0,\mathrm{C}}$ by $T_{0,d}$ by between -1.0 and -2.2 K. Generally, anisotropy is lower at night. After the hotspot disappears, most of the view directions show similar values for a given ϕ. Moving onto the morning, a hot spot develops in intensity by 08:30 and causes very large $T_{0,d}$ to ~~$T_{0,C}$ differences of -2.5~~ $T_{0,\mathrm{C}}$ differences of -2.4 K when looking from the west.

Throughout all simulations, we find overestimations of ~~$T_{0,C}$ by $T_{B,\mathrm{p}}$~~ $T_{0,\mathrm{C}}$ by $T_{0,d}$ of up to +2.9 K (17:30) and underestimations by up to ~~-2.7~~ -2.6 K (08:30) (Figure 9). The simulated values of $T_{0,d}$ can be also used to determine the anisotropy (maximum temperature difference between the most extreme view directions), which is the distance between the minimum and maximum whiskers in Figure 9.

The effective anisotropy shows expected behaviour following observational results from Voogt and Oke (1997), with high anisotropy in the daytime (up to 3.5 K) and little anisotropy at night (< 1.0 K). The trend also follows that of the residential neighborhood in Voogt and Oke (1998), which showed higher differences in measured brightness tempera-

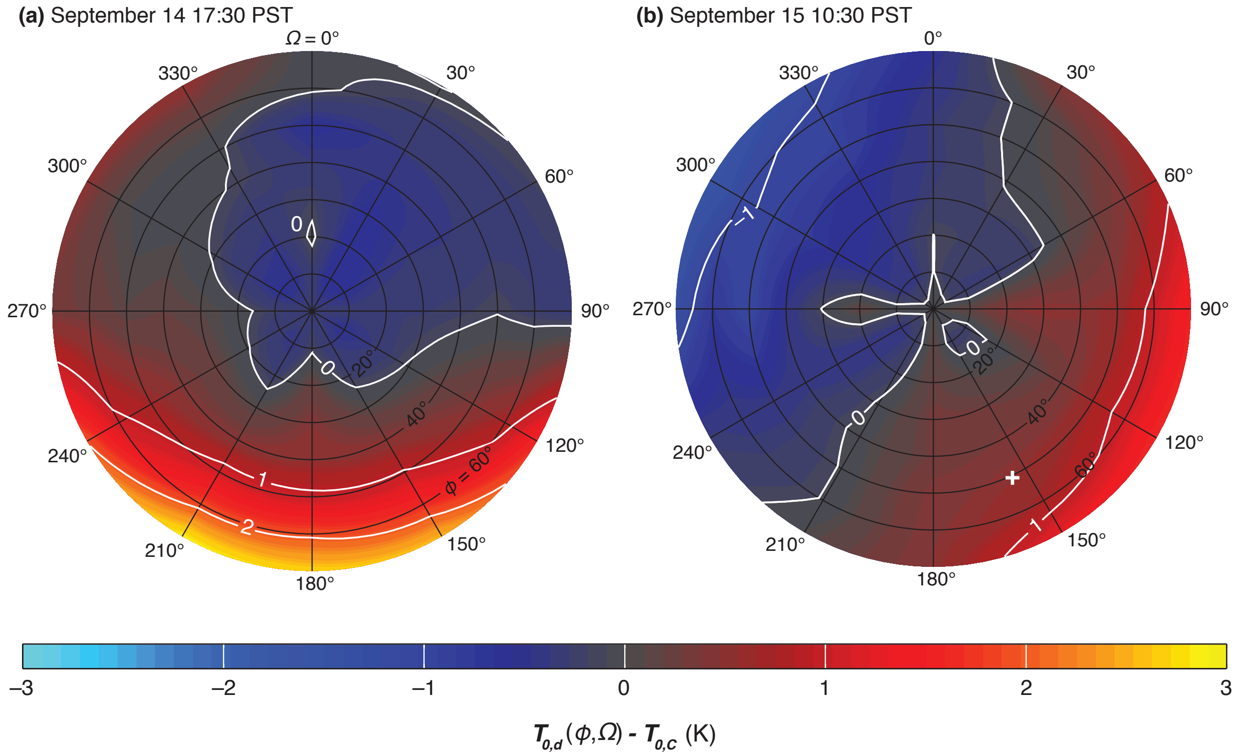

Figure 8. Examples of the bias $T_{0,d}$ - ~~$T_{0,c}$~~ $T_{0,C}$ for sensors with a narrow ~~IFOV~~ FOV in the nadir and various oblique angles one hour after sunset (left, 17:30) and in the late morning (right, 10:30). The white cross shows the relative position of the solar disk at this time. Graphs for all other hourly time steps can be found in the web-supplement to this article.

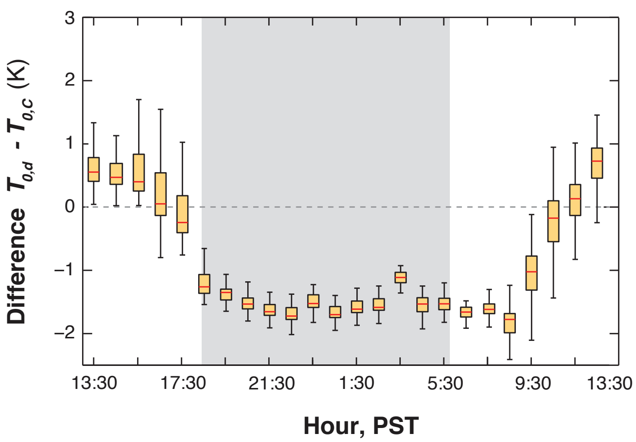

Figure 9. Deviation of all simulated view direction temperatures from ~~$T_{0,c}$~~ $T_{0,C}$ by timestep. The boxplot show minimum, maximum (whiskers), 5% and 95% percentiles (boxes) and median values (bars).

tures from differing view directions in morning and late afternoon situations (10:00 and 17:00) compared to midday situation (14:00). Magnitudes are similar as well though the simulated Elgin Street anisotropy is lower by approximately 1.5 K at 10:00 and 17:00. All of these studies took place in Vancouver neighbourhoods with similar urban structure, so an agreement is expected and supports the findings here. Aircraft measurements of thermal anisotropy from Marseille, France in Lagouarde et al. (2004) also follow this trend, with maximum anisotropy during the morning (8:00 to 10:00). However, their anisotropy is much larger (up to 10.5 K) likely due to the different urban form and fabrics~~as well as~~, different thermal sensor types, and potentially also differences in the ratio of direct to diffuse shortwave irradiance.

3.3 Hemispherical sensor

Figure 10 shows simulated signals of longwave emittance L_h measured by a hemispherical sensor (i.e. a downward facing pyrgeometer) at various locations above the canyon for the mid-day and a midnight time step.

3.3.1 Daytime case

At 13:30 there is a strong variation in L_h with pyrgeometer position across the canyon as indicated by the different coloured profiles in Figure 10a. The ~~different~~ 18 profiles converge near 500 $\mathrm{W\,m^{-2}}$ ~~well above the canyon at $z/z_b \approx 5$.~~ at $z/z_b = 7.5$ to a RMSE between all profile locations at the same height of less than 1 $\mathrm{W\,m^{-2}}$. The pattern of variability between sensor positions across the canyon cross section is repeated for all three canyon slices ($y = -30, 0, 30$ m, see Fig. 3) with only minor differences.

Below z_b, pyrgeometer positions over lawns exhibit lower L_h (lower T_0 due to transpirative cooling of lawns that cover the largest view fraction in ~~IFOV~~the FOV). The pyrgeometer positions on ~~opposide~~ opposite sides of the street exhibit different behaviour: the positions over the western lawn experience higher L_h due to the warmer nearby house east-facing walls ~~(heating all morning).~~ and also the warmer grass temperatures on the west lawns at noon (2.5 K warmer than lawns on east side). West lawns and the east-facing walls receive more incoming shortwave radiation during the morning when they are not shaded. For the pyrgeometer positions over the eastern lawn, L_h increases continuously with height, particularly above $z/z_b = 1.0$, as at this point roofs will begin to contribute to the sensor view. Being substantially warmer than lawns, the roofs will increase the measured L_h. The western lawn shows a different pattern, with rapidly increasing L_h until $z/z_b = 1.5$ at which point L_h beings to decrease with height~~until convergence is reached near $z/z_b \approx 5$.~~.

The profiles of simulated pyrgeometer positions over road and lane facets are behaving roughly similar, with the road having slightly higher temperatures due to a larger area covered by ~~asphalt~~ concrete being present and the higher ψ_{sky} of this position compared to the simulated lane. This causes L_h over the road at low z/z_b to be larger. For the lane, its lower ψ_{sky} will reduce heating due to lower solar irradiance (shadowing). In addition, facets visible in the lane include recessed areas such as garages and porches which receive less irradiance throughout the entire day. We would expect these recessed areas to reduce overall L_h. Both road and lane locations show a decrease in L_h with height.

Directly above the roofs, L_h varies greatly across the canyon and for many positions is higher than the converged value far above the canopy, as the view factor comprises mostly hot roofs while walls are less visible. Roofs have been shown to be warmer throughout the experiment in the daytime (see Figure 5), and also exhibit a range of different albedo and thermal admittance values and that explain differences along the canyon and between the east and west rows. Most profiles of L_h decrease rapidly with height~~, and again converge with other values by $z/z_b \approx 5$.~~. Just above-roof, positions over roofs show larger variability of L_h with location in the along-canyon direction as opposed to the other positions (lawns, road). This variability is driven by differences in roof materials from house to house, with asphalt roofs giving consistently higher L_h temperatures than metal roofs~~with low ε~~, likely due to differences in albedo.

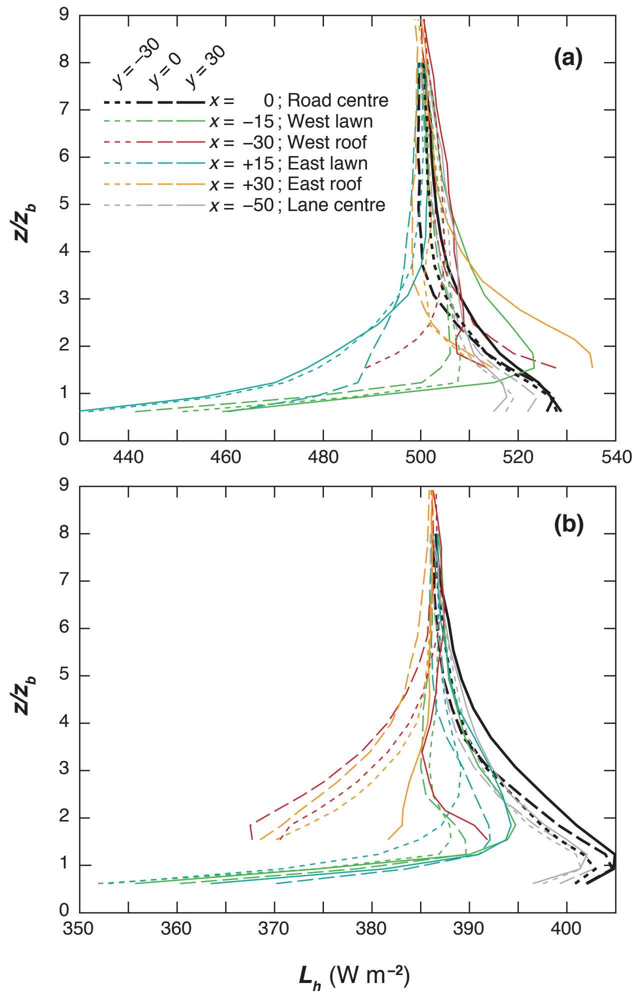

Figure 10. Simulated signals for L_h retrieved from hemispherical sensors (pyrgeometers) at various heights and locations for (a) September 14 14:00 and (b) September 15 00:30. Each graph represents a vertical profile above a specific canyon location as shown in Figure 3. Note the different scales of the x-axis in panels (a) and (b).

3.3.2 Nighttime case

At 00:30 (Figure 10b), the vertical profiles of simulated L_h (Figure 5.16) experience a similar shape for locations over the road and over lawns with a local maxima in the range $1 < z/z_b < 2$. Near-surface positions above lawns remain the lowest L_h of all profiles. Modeled L_h increases immediately and rapidly with height above the two lawn positions as warmer night-time walls come into the ~~IFOV~~ FOV of the radiometers. For both positions over lawns, L_h decreases with height above z/z_b = 1.5 as roofs come to dominate the ~~IFOV~~FOV. It is however interesting to note the variation between the profiles above the east and west lawns. Above the eastern lawn the profile of L_h decreases more slowly with height. This is likely a remnant from afternoon heating delivering irradiance to warm the west-facing walls of the eastern row of houses for longer in the evening. Cooling of house facades and lawns on the western side of the canyon has a head start, so L_h over western lawn positions decrease faster. Even with this difference, by ~~$z/z_b \approx 6.0$, all positions over lawns~~ $z/z_b = 6.3$, the RMSE between all positions converge near 387 $\mathrm{W\,m^{-2}}$. There is no significant variation in the observed profiles over lawns at the different horizontal slices.

Above roads and lanes, the profiles show that L_h is increasing until z/z_b = 1.0 and then decreasing~~to converge with other profiles at $z/z_b = 7.0$ and $L_h = 387\ \mathrm{W\,m^{-2}}$~~. There is no significant variation in the observed profiles over roads and lanes at the three different along-canyon cross-sections.

Above-roofs, L_h shows substantial variation depending on position ~~in the canyon~~ along the canyon due to different daytime heating (albedo) and thermal admittance (roof isolation). In general however the magnitude of the variation is less than during the daytime: temperature differences between different roofs are lower. Profiles of L_h above western houses show an increase with height until convergence with ~~other profiles near~~ all other profiles at z/z_b = ~~6.0~~6.3.

3.4 Impact on radiometer placement

All simulated pyrgeometer positions from all modelled timesteps show convergence of L_h with height. The overall RMSE value between the 18 different locations at each time step and height is shown in Table 4. It is assumed the 18 positions cover a large enough sample of horizontal variability. To measure a consistent L_h regardless of location with a typical positional error of < 1, < 5 and $< 10\ \mathrm{W\,m^{-2}}$ a hemispherical pyrgeometer would have to be placed at $z/z_b > 7.5$, > 4.0 and > 2.4 respectively during daytime. At night, the curves fall < 1, < 5 and $< 10\ \mathrm{W\,m^{-2}}$ at $z/z_b > 6.3$, > 3.2 and > 1.9, respectively. The RMSE between the different horizontal positions as a function of height is well approximated by an exponential formulation:

$$\mathrm{RMSE} = a\exp(-b\,z/z_b) \tag{7}$$

Table 4. RMSE of selected horizontal positions for increase in radiometer altitude. Road positions are not included.

z (m)	z/z_b	RMSE 13:30 ($\mathrm{W\,m^{-2}}$)	RMSE 18:30 ($\mathrm{W\,m^{-2}}$)	RMSE 00:30 ($\mathrm{W\,m^{-2}}$)	RMSE 06:30 ($\mathrm{W\,m^{-2}}$)
8	1.28	20.2	14.9	11.2	9.2
12	1.93	14.9	9.3	11.1	10.8
16	2.57	9.6	6.5	8.5	8.4
20	3.21	6.2	3.8	5.8	5.7
24	3.85	4.4	2.6	3.8	3.8
28	4.49	3.4	1.8	2.5	2.5
32	5.14	2.8	1.5	1.6	1.7
36	5.78	2.3	1.1	1.1	1.2
40	6.42	1.8	0.83	0.78	0.86
44	7.06	1.4	0.56	0.62	0.68
48	7.70	1.1	0.46	0.44	0.52
52	8.35	0.85	0.36	0.34	0.41
58	9.31	0.53	0.32	0.28	0.34

where b is a coefficient that describes the rate of convergence relative to mean building height, and a is ~~the RMSE at $z/z_b = 1.0$~~ a coefficient that describes the hypothetical RMSE at ground level ($z/z_b = 0$) in $\mathrm{W\,m^{-2}}$. In the current case, b seems invariant with time for all four time steps simulated at $b = 0.475$ ($R^2 = 0.991$). Practically, a is roughly proportional to the ~~standard deviation of T_0~~ RMSE of the sub-facet $L_{uparrow}$ of the complete urban surface and is highest during daytime ($\approx 30\ \mathrm{W\,m^{-2}}$) and lower in the evening and morning transition periods ($\approx 20\ \mathrm{W\,m^{-2}}$).

In terms of horizontal location, convergence occurs more rapidly above locations that are either road or lawns; a radiometer positioned at z/z_b = 5 would record a flux within 1.5 $\mathrm{W\,m^{-2}}$ of the convergent value. This means pyrgeometers are more representative for the neighbourhood average in this area when installed over the canyon compared to over roofs, explained by the energy balance and geometric structure of these two extremes. The preferred location to create the most representative sample already at lower heights would be halfway in between the canyon/lanes and roofs.

The differences between horizontal positions shown here are much larger than Roberts (2010) found using a scale model of a idealized urban canopy in a hardware scale model. This indicates that the large variation present in upwelling longwave radiation with horizontal location is also driven by ~~material and facet variability~~facet-scale variability on material and geometry, as the scale model of Roberts (2010) had low material variation and a repetitive geometry. Voogt (2008) demonstrates the importance of microscale temperature variability due to varying material properties on the effective anisotropy of an urban canopy. The regular geometry and uniform material of an idealized urban surface in a controlled scale experiment may miss a significant fraction of the effective anisotropy. A simulation done by Hénon et al.

(2011) using the SOLENE model for a ~~realsitic~~ realistic urban fragment in Marseille with increased detail found larger differences (up to 20% of the value of L_h) between horizontal locations at z/z_b = 1.5 but they found that differences in L_h were insignificant at z/z_b = 2.5. This is a lower height than that calculated here, and may be due to the greater building density of Marseille compared to the open-set Vancouver Sunset morphology, as well as wider material differences of the facets in the current study (no extensive lawns in Marseille). Increased building density reduces the view factor of walls and the lack of lawns changes the thermal properties of the ground.

3.5 Hemispherical radiometric temperature

In some applications it is helpful to express measured L_h as a hemispherical radiometric temperature $T_{0,h}$ (Norman and Becker, 1995). $T_{0,h}$ was calculated in absence of emissivity effects inverting the Stefan- Boltzmann law $(T_{0,h}/\sigma)^{0.25}$ (i.e. using $\varepsilon = 1.0$). Then $T_{0,h}$ was compared to ~~$T_{0,C}$~~ $T_{0,\mathrm{C}}$ and $T_{0,d}(\phi = 0)$ for a nadir view in the four timesteps examined (with $T_{0,h}$ being averaged at $z/z_b = 8$ over all 18 profiles). Surprisingly, the directional radiometric surface temperature in the nadir, $T_{0,d}(\phi = 0)$, appears to be a better estimator for ~~$T_{0,C}$~~ $T_{0,\mathrm{C}}$ than $T_{0,h}$. The RMSE for $T_{0,d}(\phi = 0)$ - ~~$T_{0,C}$~~ $T_{0,\mathrm{C}}$ over the 24 hour cycle is computed as 1.4 K, while the RMSE for $T_{0,h}$ - ~~$T_{0,C}$~~ $T_{0,\mathrm{C}}$ is higher at 1.8 K.

4 Summary and conclusions

A methodology was developed and successfully applied to simulate the measurement bias of different remote sensors when inferring longwave emittance and surface temperatures of a convoluted, three dimensional urban surface. Unlike previous observational studies, mostly based on helicopter or aircraft measurements (e.g. Lagouarde et al., 2004; Sugawara and Takamura, 2006), the current methodology allows a high repetition in time and a spatial resolution at the sub-facet scale.

The bias of various ~~IFOVs~~ FOVs (nadir, hemispherical, oblique) was quantified. The methodology was based on a panoramic time sequential thermography dataset (PTST) recorded over a 24h cycle using a thermal camera on a hydraulic mast in an urban street canyon~~in Vancouver, BC, Canada~~. Methods from micrometeorology, computer vision and computer graphics were combined to project the PTST onto a detailed, photogrammetrically-derived 3D model of the urban structure surrounding the hydraulic mast, then corrected for atmospheric and emissivity effects to retrieve T_0 at sub-facet scale. Facets of the 3D model that were not seen by the thermal camera were statistically gap-filled with data from other areas based on selected predictors (ψ_{sky}, material, orientation of facet). The resulting three dimensional model allowed the computation of the complete surface temperature ~~$T_{0,C}$~~ $T_{0,\mathrm{C}}$ and the simulation of the directional and hemispherical radiometric surface temperatures in absence of emissivity effects at varying locations and orientations in and above the canyon.

Simulated directional radiometric surface temperatures for the various sensors showed that none were properly able to record the true complete surface temperature, and all experienced biases. Deviations between ~~-2.2~~ -1.9 K (day) and +1.6 K (night) were found between the directional radiative surface temperature in the nadir, $T_{0,d}(\phi = 0)$, and ~~$T_{0,C}$~~ $T_{0,\mathrm{C}}$. For simulated off-nadir view directions, the deviation between $T_{0,d}(\phi, \Omega)$ and ~~$T_{0,C}$~~ $T_{0,\mathrm{C}}$ was larger; ranging from ~~-2.7~~ -2.6 to +2.9K. The effective thermal anisotropy of the surface was highest in the daytime (particularly at sunrise and sunset, up to 3.5 K) which is consistent with the literature. The effective thermal anisotropy in this study was similar in form but lower in magnitude to that measured over a residential area in Vancouver in Voogt and Oke (1998) (near 8 K in their study). The same pattern of a east-west effective thermal anisotropy following the street canyon orientation was reproduced in the current study.

The results are valid for a suburban surface without tall vegetation. In this regard, the selected study canyon is quite unusual. Dyce (2014) modelled a larger subset of the same neighborhood including the canyon section investigated here (called Vancouver-Sunset 'NW Subdomain' in Dyce (2014)). His model incorporates the effects of tall vegetation. Modelled estimates of anisotropy suggest the tree-free effective anisotropy to be 2.1K (1200 LMST) and 2.4 K (0900 LMST). However when trees are added the effective anisotropy increased to 4.7 and 2.8 K respectively.

The hemispherical sensor simulations showed that the proper placement of a hemispherical downward facing pyrgeometer above a city is critical to measure an outgoing longwave radiation flux density $L_\uparrow$ that is representative for the entire urban canopy. The average horizontal positional error for a sensor at 2, 3 and 5 times the mean building height z_b was 11.2, 6.3 and 2.0 Wm^{-2}. The positional error between different horizontal locations in retrieving $L_\uparrow$ decreased exponentially with height. Generally above $3.5\,z_b$ the horizontal positional error was less than the typical accuracy of high-quality pyrgeometers ($\pm 5\mathrm{Wm}^{-2}$).

The approach taken in the paper could easily be extended to other urban morphometries, geographic locations and different wavebands (e.g. albedo). The equipment needed is relatively simple - a scanning (spectral) imaging system and a detailed USM. To increase the coverage, several systems on multiple towers or ground locations could reduce the need for gap-filling. Also, the gap-filling algorithm could be improved by incorporating the effects of facet shading and shading history, which are both currently not considered as selection criteria in the search for similar cases to fill gaps.

It might be possible to develop empirical correction factors to allow estimation of ~~$T_{0,C}$~~ $T_{0,\mathrm{C}}$ from $T_{0,d}$. However, it is likely that these factors would be unique to a particular geometry and might only be applicable in the neighborhood/city that they were created in.

An interesting theoretical question that remains is the choice of the appropriate bulk-surface temperature of an urban canopy in one-dimensional urban surface parameterizations. While the energy balance of the UCL is greatly controlled by $T_{0,f}$ of the canyon walls and floor, the roof temperature may be less important to most of the UCL. Many multilayer urban surface parameterization specifically model $T_{0,f}$ of individual facets (walls, ground, roof) (Grimmond et al., 2010). But the surface temperature 'seen' from a layer in the atmosphere above the city is also not simply adding the roofs to get the the complete surface temperature ~~$T_{0,C}$~~ $T_{0,C}$, but rather the hemispherical radiometric temperature $T_{0,h}$. This work also showed that $T_{0,C} \neq T_{0,h}$, because the relative weighting (view factors) are different for a hemispherical sensor compared to the pure area-weighting of the complete urban surface.

Acknowledgements. This study was supported by the Canadian Foundation for Climate and Atmospheric Sciences (CFCAS) as part of the Network Grant 'Environmental Prediction in Canadian Cities' (EPiCC) and by NSERC Discovery Grants (A. Christen, J. A. Voogt). Selected equipment was provided by Environment Canada. Dr. Fred Meier (Technische Universität Berlin) provided MODTRAN runs for atmospheric corrections in the specific context. Dr. Nicholas Coops (UBC Forestry) and his research group provided processed LiDaR surface data and Dr. Bob Woodham (UBC Computer Science) provided technical assistance. F. Chagnon, B. Crawford, A. Jones, R. Ketler, K. Liss, T. Oke, C. Siemens, and D. van der Kamp helped with the planning, infrastructure and/or field work of PTST data acquisition. We thank E. Leinberger for drawing ~~most~~ figures.

References

Adderley, C. D.: The effect of preferential view direction on measured urban surface temperature, Master's thesis, University of British Columbia, 2012.

Arya, S. P.: Introduction to Micrometeorology, Academic Press, 2 edn., 2008.

Christen, A. and Vogt, R.: Energy and radiation balance of a central European city, International Journal of Climatology, 24, 1395–1421, 2004.

Christen, A., Meier, F., and Scherer, D.: High-frequency fluctuations of surface temperatures in an urban environment, Theoretical and Applied Climatology, 108, 301–324, 2012.

Christen, A., Oke, T. R., Steyn, D. G., and Roth, M.: 35 years of urban climate research at the 'Vancouver-Sunset' flux tower, FluxLetter, 5, 29–36, 2013.

Chudnovsky, A., Ben-Dor, E., and Saaroni, H.: Diurnal thermal behavior of selected urban objects using remote sensing measurements, Energy and Buildings, 36, 1063–1074, 2004.

Cleugh, H. A. and Oke, T. R.: Suburban-rural energy balance comparisons in summer for Vancouver, Boundary-Layer Meteorology, 36, 351–369, 1986.

Dyce, D. R.: A sensor view model to investigate the influence of tree crowns on effective urban thermal anisotropy, Master's thesis, The University of Western Ontario, London, ON, 2014.

Flir Systems: ThermoVision A40M operator's manual , 2004.

Goodwin, N. R., Coops, N. C., Tooke, T. R., Christen, A., and Voogt, J. A.: Characterizing urban surface cover and structure with airborne lidar technology, Canadian Journal of Remote Sensing, 35, 297–309, 2009.

Grimmond, C. S. B., Blackett, M., Best, M., Barlow, J., Baik, J., Belcher, S. E., Bohnenstengel, S. I., Calmet, I., Chen, F., Dandou, A., Fortuniak, K., Gouvea, M. L., Hamdi, R., Hendry, M., Kawai, T., Kawamoto, Y., Kondo, H., Krayenhoff, E. S., Lee, S. H., Loridan, T., Martilli, A., Masson, V., Miao, S., Oleson, K., Pigeon, G., Porson, A., Ryu, Y. H., Salamanca, F., Shashua-Bar, L., Steeneveld, G. J., Tombrou, M., Voogt, J. A., Young, D. T., and Zhang, N.: The International Urban Energy Balance Models Comparison Project: First results from Phase 1, Journal of Applied Meteorology and Climatology, 49, 1268–1292, 2010.

Harman, I., Best, M., and Belcher, S. E.: Radiative exchange in an urban street canyon, Boundary-Layer Meteorology, 110, 301–316, 2004.

Hénon, A., Mestayer, P. G., Groleau, D., and Voogt, J.: High resolution thermo-radiative modeling of an urban fragment in Marseilles city center during the UBL-ESCOMPTE campaign, Building and Environment, 46, 1747–1764, 2011.

Johnson, G. T. and Watson, I. D.: The determination of view-factors in urban canyons, Journal of Climate and Applied Meteorology, 23, 329–335, 1984.

Kotthaus, S., Smith, T. E. L., Wooster, M. J., and Grimmond, C. S. B.: Derivation of an urban materials spectral library through emittance and reflectance spectroscopy, ISPRS Journal of Photogrammetry and Remote Sensing, 94, 194–212, 2014.

Krayenhoff, E. S., Christen, A., Martilli, A., and Oke, T. R.: A multi-layer radiation model for urban neighbourhoods with trees, Boundary-Layer Meteorology, 151, 139–178, 2014.

Lagouarde, J., Moreau, P., Irvine, M., Bonnefond, J., Voogt, J. A., and Solliec, F.: Airborne experimental measurements of the angular variations in surface temperature over urban areas: case study of Marseille (France), Remote Sensing of Environment, 93, 443–462, 2004.

Lagouarde, J. P., Henon, A., Kurz, B., Moreau, P., Irvine, M., Voogt, J., and Mestayer, P.: Modelling daytime thermal infrared directional anisotropy over Toulouse city centre, Remote Sensing of Environment, 114, 87–105, 2010.

Masson, V., Grimmond, C. S. B., and Oke, T. R.: Evaluation of the Town Energy Balance (TEB) Scheme with Direct Measurements from Dry Districts in Two Cities, Journal of Applied Meteorology, 41, 1011–1026, 2002.

Meier, F., Scherer, D., Richters, J., and Christen, A.: Atmospheric correction of thermal-infrared imagery of the 3-D urban environment acquired in oblique viewing geometry, Atmospheric Measurement Techniques, 4, 909–922, 2011.

Nikiforiadis, F. and Pitts, A.: 3D digital geometric reconstruction of the urban environment for daylight simulation studies, in: Eighth International Building Simulation Conference, Eindhoven, 2003.

Norman, J. M. and Becker, F.: Terminology in thermal infrared remote-sensing of natural surfaces, Agricultural and Forest Meteorology, 77, 153–166, 1995.

Offerle, B. D., Grimmond, C. S. B., Fortuniak, K., and Pawlak, W.: Intraurban differences of surface energy fluxes in a central European city, Journal of Applied Meteorology, 45, 125–136, 2006.

Oke, T. R.: Canyon geometry and the nocturnal urban heat island: Comparison of scale model and field observations, International Journal of Climatology, 1, 237–254, 1981.

Oke, T. R.: The energetic basis of the urban heat-island, Quarterly Journal of the Royal Meteorological Society, 108, 1–24, 1982.

Oke, T. R.: Boundary Layer Climates, 1987.

Roberts, S. M.: Three-dimensional radiation flux source areas in urban areas, Ph.D. thesis, University of British Columbia, 2010.

Salmond, J. A., Roth, M., Oke, T. R., Christen, A., and Voogt, J. A.: Can Surface-Cover Tiles Be Summed to Give Neighborhood Fluxes in Cities?, Journal of Applied Meteorology and Climatology, 51, 133–149, 2012.

Shirley, P., Ashikhmin, M., and Marschner, S.: Fundamentals of Computer Graphics, 2009.

Stewart, I. D. and Oke, T. R.: Local climate zones for urban temperature studies, Bulletin of the American Meteorological Society, 93, 1879–1900, 2012.

Sugawara, H. and Takamura, T.: Longwave radiation flux from an urban canopy: Evaluation via measurements of directional radiometric temperature, Remote Sensing of Environment, 104, 226–237, 2006.

Voogt, J. A.: Assessment of an urban sensor view model for thermal anisotropy, Remote Sensing of Environment, 112, 482–495, 2008.

Voogt, J. A. and Oke, T. R.: Complete urban surface temperatures, Journal of Applied Meteorology, 1997.

Voogt, J. A. and Oke, T. R.: Radiometric temperatures of urban canyon walls obtained from vehicle traverses, Theoretical and Applied Climatology, 60, 199–217, 1998.

Voogt, J. A. and Oke, T. R.: Thermal remote sensing of urban climates, Remote Sensing of Environment, 86, 370–384, 2003.